Check for updates

# Independent component analysis for reservoir geomorphology and unsupervised seismic facies classification in the Taranaki Basin, New Zealand

David Lubo-Robles[1] and Kurt J. Marfurt[1]


## Abstract

During the past two decades, the number of volumetric seismic attributes has increased to the point at which interpreters are overwhelmed and cannot analyze all of the information that is available. Principal component analysis (PCA) is one of the best-known multivariate analysis techniques that decompose the input data into second-order statistics by maximizing the variance, thus obtaining mathematically uncorrelated components. Unfortunately, projecting the information in the multiple input data volumes onto an orthogonal basis often mixes rather than separates geologic features of interest. To address this issue, we have implemented and evaluated a relatively new unsupervised multiattribute analysis technique called independent component analysis (ICA), which is based on higher order statistics. We evaluate our algorithm to study the internal architecture of turbiditic channel complexes present in the Moki A sands Formation, Taranaki Basin, New Zealand. We input 12 spectral magnitude components ranging from 25 to 80 Hz into the ICA algorithm and we plot 3 of the resulting independent components against a red-green-blue color scheme to generate a single volume in which the colored independent components correspond to different seismic facies. The results obtained using ICA proved to be superior to those obtained using PCA. Specifically, ICA provides improved resolution and separates geologic features from noise. Moreover, with ICA, we can geologically analyze the different seismic facies and relate them to sand- and mud-prone seismic facies associated with axial and off-axis deposition and cut-and-fill architectures.


## Introduction

In addition to picking horizons, traditional interpretation includes the identification of geologic features of interest such as faults, collapse features, channel complexes, salt domes, and mass transport deposits in 3D seismic amplitude volumes. Volumetric seismic attributes such as coherence, curvature, gray-level co-occurrence matrix texture attributes, and spectral-decomposition analysis can accelerate and facilitate this process, enhancing subtle features that may otherwise be overlooked. Depending on the seismic attributes interpreter's selection, different information is extracted (Infante-Paez and Marfurt, 2017; Infante-Paez, 2018). Therefore, relying solely on a single attribute can lead to an incomplete seismic interpretation in which important geologic elements can be overlooked. During the past two decades, the number of volumetric seismic attributes has increased to the point at which interpreters are overwhelmed and cannot analyze all of the information available.

Corendering using red-green-blue (RGB) or hue-lightness-saturation color gamuts provides an efficient means of combining the information content of three volumes. For more than three volumes, one may project the higher dimensional data onto a lower dimensional space. Principal component analysis (PCA) (Guo et al., 2009; Chopra and Marfurt, 2014; Roden et al., 2015; Zhao et al., 2015) organizes multivariate data into linearly uncorrelated components using second-order statistics based on the covariance matrix of the data. The first three components are either corendered using RGB or interpreted using crossplotting tools. PCA is also widely used as the first iteration for clustering techniques to reduce the dimensionality of the input data (Zhao et al., 2015; Sinha et al., 2016). The $k$-means algorithm (MacQueen, 1967) is a clustering technique in which, after the interpreter decides the number of desired clusters, the distance between the multiattribute data point and the center of the clusters is measured using the Mahalanobis distance. Each data point is associated with the closest cluster (Zhao et al., 2015). Generative topographic maps generate a probabilistic representation of the data on a lower dimensional manifold (Roy et al., 2014; Zhao et al., 2015). Perhaps the

[1]The University of Oklahoma, School of Geology and Geophysics, Norman, Oklahoma, USA. E-mail: davidlubo@ou.edu; kmarfurt@ou.edu.

Manuscript received by the Editor 16 June 2018; revised manuscript received 24 August 2018; published ahead of production 08 February 2019; published online 11 April 2019. This paper appears in *Interpretation*, Vol. 7, No. 3 (August 2019); p. SE19–SE42, 26 FIGS.
http://dx.doi.org/10.1190/INT-2018-0109.1. © 2019 Society of Exploration Geophysicists and American Association of Petroleum Geologists. All rights reserved.



Downloaded 07/31/19 to 68.97.115.26. Redistribution subject to SEG license or copyright; see Terms of Use at http://library.seg.org/

most widely used clustering technique is self-organizing maps (SOMs), in which a lower dimensional manifold is first deformed to represent the data that in turn are projected onto a corresponding latent space (Kohonen 1982; Strecker and Uden, 2002; Coléou et al., 2003; Zhao et al., 2015, 2016; Marfurt, 2018).

Spectral-decomposition analysis (Sinha et al., 2005; Chopra and Marfurt, 2016) decomposes the seismic volume into a suite of magnitude and phase components at different frequencies that allow the study of geologic features near the limits of seismic resolution, enabling the interpreter to map lateral changes in thickness, lithology, and porosity. A major drawback in spectral-decomposition analysis is that, from one 3D amplitude volume, one may generate up to 10–100 output volumes (Guo et al., 2009), making the selection and visualization of the most important components a cumbersome task. Guo et al. (2009) apply PCA to characterize channels draining an unconformity in the Central Basin Platform in Texas, and Li et al. (2009) apply independent component analysis (ICA) to a carbonate bank data volume to map reef as well as shoaling features. Honorio et al. (2014) apply ICA to a fluviodeltaic system to map channels.

Inspired by Honorio et al.'s (2014) work, we implemented our own ICA algorithm and applied it to a deepwater turbidite system in the Taranaki Basin, New Zealand, and we compared the results not only to the input data volumes, but also to the more commonly used corendered PCA volume.

To illustrate ICA, we consider the popular cocktail-party problem, in which two people are speaking simultaneously in a room where two microphones record the combination of their voices (Figure 1). The recorded signals $\mathbf{X} = \{\mathbf{X_1}, \mathrm{X_2}\}$ are a linear mixture of the people's voices $\mathbf{P} = \{\mathbf{P_1}, \mathbf{P_2}\}$, which can be written as

$$\mathbf{X} = \mathbf{AP}, \tag{1}$$

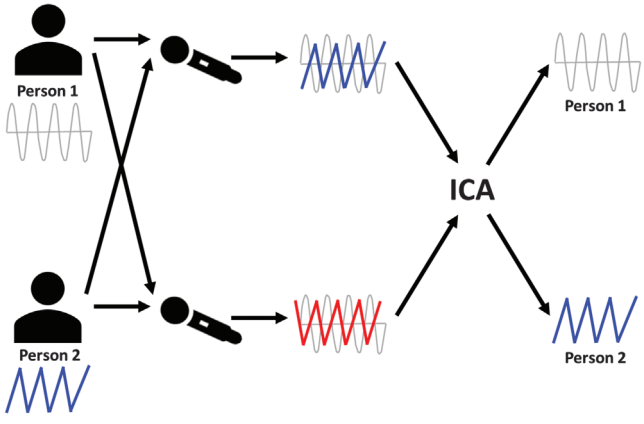


**Figure 1.** Illustration of ICA using the popular cocktail-party problem. The goal is to recover the individual signals $\mathbf{P_1}$ and $\mathbf{P_2}$ from the mixtures signals $\mathbf{X_1}$ and $\mathbf{X_2}$.

where $\mathbf{A}$ is an unknown matrix called the mixing matrix, whose parameters are a function of the distances between the microphones and the speakers.

Although the goal is to estimate the people's voices $\mathbf{P_1}$ and $\mathbf{P_2}$, the matrix $\mathbf{A}$ is unknown, such that $\mathbf{P_1}$ and $\mathbf{P_2}$ cannot be computed directly from $\mathbf{X}$. ICA assumes that the components $\mathbf{P_i}$ are statistically independent, allowing the computation of the matrix $\mathbf{A}$ and its inverse $\mathbf{W}$ (Hyvärinen and Oja, 2000):

$$\mathbf{P} = \mathbf{WX}. \tag{2}$$

The cocktail-party problem is analogous to our objective in mapping the Moki A sands Formation of the Taranaki Basin in New Zealand. Rather than having two measurements of two simultaneous human speakers, we have $N$-spectral component measurements of an unknown number of geologic facies that are mixed in the seismic response measured by $M$ traces. Within a given target, we hypothesize that a given geologic speaker will exhibit the same spectrum across the survey. Our goal is to use ICA to not only better delineate but also to determine how many geologic sources are needed to statistically represent the measured data.

In this study, we begin with an explanation of the differences between PCA and ICA techniques. Using an ICA algorithm developed by Hyvärinen and Oja (2000) for feature extraction and signal separation as a guide, we implement an ICA algorithm that can work on a suite of large, 3D volumetric seismic attributes. The choice of attributes used depends on the geologic target. To study submarine turbidites in the Moki A sands of the Taranaki Basin, New Zealand, we use spectral magnitude components that are routinely used to image fluvial and deepwater channel and canyon systems (e.g., Partyka et al., 1999; Marfurt and Kirlin, 2001; Lubo-Robles and Marfurt, 2017). We then analyze these spectral components individually and as input to the PCA and ICA algorithms. We conclude with a discussion of the ICA and its advantages with respect to the well-established PCA. Finally, we add Appendix A with mathematical details explaining how the algorithm works.

## Theory

A principal component is a scalar value that represents the projection of an $N$-dimensional sample vector, against an $N$-dimensional eigenvector. This technique is known as PCA, and, based on Gaussian statistics, it decomposes the data into mathematically linearly uncorrelated components. PCA reduces the dimensionality and redundancy of the input multivariate data, but it may omit geologic features associated with lower reflectivity (Guo et al., 2009). PCA is based on an assumption that the data exhibit Gaussian statistics, allowing the use of second-order statistics to decompose the data into orthogonal components sorted based on their variability. Principal components are ranked according to the energy of the input data they represent.

Downloaded 07/31/19 to 68.97.115.26. Redistribution subject to SEG license or copyright; see Terms of Use at http://library.seg.org/

Downloaded 07/31/19 to 68.97.115.26. Redistribution subject to SEG license or copyright; see Terms of Use at http://library.seg.org/

In contrast to PCA, ICA is based on higher order statistics, and it separates a multivariate signal into independent, but not necessarily orthogonal, subcomponents, finding a linear representation of non-Gaussian data (Hyvärinen and Oja, 2000). The concept of "independence" provides a means to capture more interesting information from the multivariate data (Honorio et al., 2014). The independent components are not only nonorthogonal, but their order is undefined (Figure 2); i.e., the independent components cannot be ranked (Hyvärinen and Oja, 2000; Tibaduiza et al., 2012).

The independent component algorithm that we propose (Figure 3) is based on the FastICA algorithm developed by Hyvärinen and Oja (2000), with modifications to implement it using volumetric seismic attributes. In our workflow, we first select the seismic attributes $\mathbf{a}$ based on the geologic features of interest and compute their means $\boldsymbol{\mu}$ and standard deviations $\boldsymbol{\sigma}$ to apply $Z$-score normalization. We compute the correlation matrix $\mathbf{C}$ from the scaled parameters and compute its eigenvectors and eigenvalues. To be computationally efficient, we decimate the data to create a representative data subset $\mathbf{a}_{\mathbf{tr}}$ from which the unmixing matrix $\mathbf{W}$ is computed.

After $Z$-normalizing the data subset $\mathbf{a}_{\mathbf{tr}}$ to avoid issues related to different units of the seismic attributes, the data are whitened and filtered using PCA (Stanford, 2018) whereby the eigenvalues retained just exceeding a choosing criterion of 90% are considered to be signal, and the others to be noise, therefore reducing the dimensionality of the multivariate data.

To initialize the algorithm, we must assume an initial guess for the unmixing matrix $\mathbf{W}$. Instead of using a random initial guess, we generate an initial guess based on the eigenvectors and eigenvalues of the correlation matrix $\mathbf{C}$ to guarantee the exact repeatability of the process.

Gaussian behavior implies maximum entropy. In ICA, the unmixing matrix $\mathbf{W}$ is estimated by maximizing the non-Gaussian behavior of the multivariate data measured by an approximation of negentropy (Hyvärinen and Oja, 2000). PCA assumes that the distributions of the input sources are Gaussian. Walden (1985) and Honorio et al. (2014) find that seismic data can be considered to be super-Gaussian distributions characterized by a positive kurtosis. In contrast, seismic attributes such as the Sobel filter similarity, coherence, and spectral magnitude components exhibit a Poisson distribution characterized by nonnegative values that is inconsistent with the unbounded support representative of a Gaussian distribution (Ma, 2011). Therefore, maximizing non-Gaussianity captures valuable information associated with higher moments of the distribution that can be used to recover the underlying independent geologic sources. Finally, when convergence is reached, the independent components are computed by projecting the $Z$-normalized and whitened seismic attributes onto the final unmixing matrix $\mathbf{W}$ obtained from the algorithm. For more information on the mathematical details of the procedure, please refer to Appendix A.

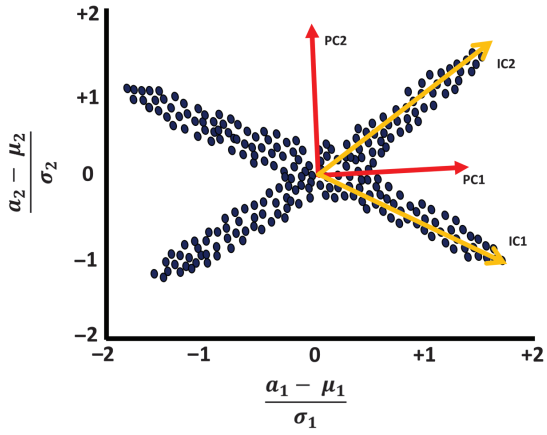


**Figure 2.** Differences between PCA and ICA. Attributes $\mathbf{a}_1$ and $\mathbf{a}_2$ are scaled by their means and standard deviations. The first eigenvector $\mathbf{v}_1$ is a line that least-squares fit the data cloud and best represent the variance of the data. PC1 is a projection of each data point onto $\mathbf{v}_1$. The second eigenvector $\mathbf{v}_2$ is a perpendicular to $\mathbf{v}_1$ and for two dimensions these two eigenvectors best represents the data. In contrast, the independent components IC1 and IC2 are latent variables whose order is undefined and are not orthogonal to each other (Hyvärinen and Oja, 2000; Tibaduiza et al., 2012). To compute the independent components, each data point is projected onto the whitened eigenvectors $\mathbf{v}_1$ and $\mathbf{v}_2$ and then projected onto the unmixing matrix $\mathbf{W}$.

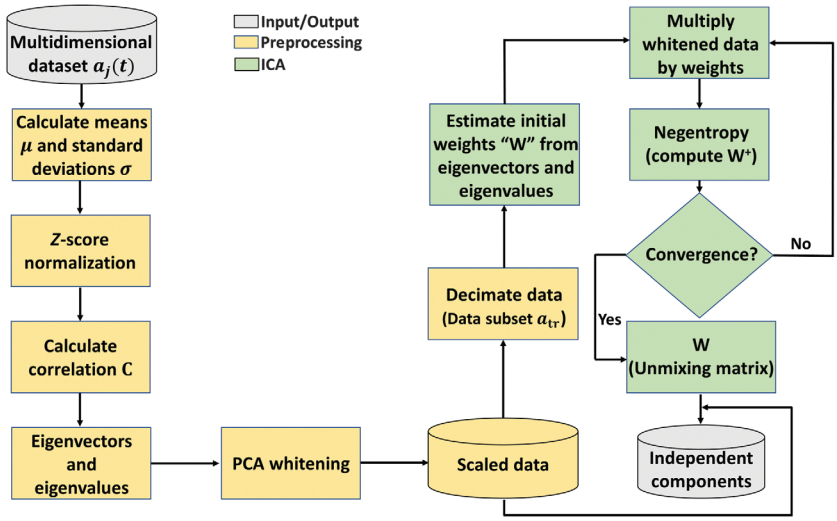


**Figure 3.** The ICA. The algorithm is based on the FastICA algorithm developed by Hyvärinen and Oja (2000), but with modifications for volumetric seismic attribute application.

Downloaded 07/31/19 to 68.97.115.26. Redistribution subject to SEG license or copyright; see Terms of Use at http://library.seg.org/

## Geologic background

The Taranaki Basin is a sedimentary basin located along the western side of the North Island, New Zealand (Palmer, 1985) (Figure 4a). The eastern Taranaki Graben Complex and the Western Platform are the two main structural elements of the basin (Pilaar and Wakefield, 1984).

The Western Platform, with a width of more than 100 km, is characterized by 2000–5000 m of Late Cretaceous-Recent sediments, and it represents the offshore part of the Taranaki Basin (Palmer, 1985). The Western Platform was affected by normal block faulting during the Late Cretaceous-Eocene, but during most of the Tertiary it remained relatively stable (Pilaar and Wakefield, 1984). The Taranaki Graben structure is controlled by movement in the basement and faults developed during the Late Cretaceous-Eocene (Palmer, 1985) with its infill characterized by sedimentary and igneous rocks (Pilaar and Wakefield, 1984).

The Taranaki Basin was initially formed by transcurrent rifting during the Late Cretaceous. Throughout this time, transgressive marine and terrestrial sedimentary rocks of the Pakawau Group were deposited (Thrasher, 1992). The Pakawu Group can be subdivided into the Rakopi and the North Cape Formations. An important characteristic of the Rakopi Formation is that it was deposited under fluvial-lacustrine conditions and has good hydrocarbon source potential (Figure 4b) (Dauzacker et al., 1996).

The Paleocene to Lower Oligocene is characterized by the deposition of the Kapuni Group, a sequence of sandstones, coal, and mudstones lithologies, which overlie the Pakawau Group after a period of transgression. Contrary to the Pakawau Group, the Kapuni Group sedimentation is distributed across all the Taranaki Basin and is not confined only to the Cretaceous Grabens (De Bock, 1994).

After the deposition of marine siltstones and mudstones related to the Turi Formation in the Eocene to Early Oligocene, the Tikorangi Limestone, a bioclastic limestone sequence, was deposited widely in the Taranaki Basin during the Oligocene, and according to De Bock (1994) it represents a regional seismic marker.

The Miocene deposits are characterized by detrital sedimentation associated with relative sea-level fluctuations and tectonism associated with deposition of sediments in the South Taranaki Graben during the Early Miocene and reverse faulting in the South Taranaki Graben during the Late Miocene (De Bock, 1994). Deposition started with deepwater mudstones and siltstones represented by the Lower Manganui Formation. In the Early to Middle Miocene, deposition of submarine fans occurred associated with a major regression (De Bock, 1994). These submarine fans were deposited on the basin floor or at the base of continental slope (Dauzacker et al., 1996) and are represented by the Mt Messenger and Moki Formations (Figure 4b). These sandstone turbidites are diachronous toward the north (Dauzacker et al., 1996).

During the Middle to Late Miocene, the Moki Formation was buried by progradational deposits of the (Upper) Manganui Formation (Dauzacker et al., 1996). The end of the Miocene was characterized by a sea-level falling stage, depositing a sequence of prograding strata known as the Giant Foresets Formation. Pliocene to present-day sediments are associated with marine deposition (De Bock, 1994).

The Moki Formation is a fine-grained turbidite sequence (Engbers, 2002), and it is comprised of sandstones interbedded with siltstone, bathyal claystone, and thin limestones (Bussell, 1994). The Moki Formation can be subdivided into the Moki A sands, the Moki B shale, and the Moki B sands (Bussell, 1994). The Moki B sands form the lower unit in the Moki Formation and consist of turbidite sheet sands with large laterally extension, which were deposited on a basin floor (Engbers, 2002). The Moki B shale represents a period of low

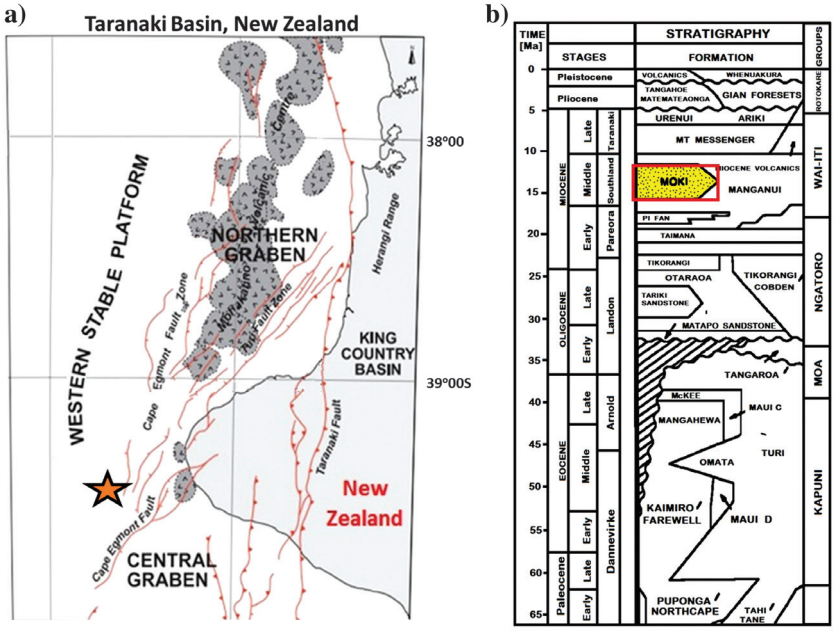


**Figure 4.** (a) The Taranaki Basin can be divided in the Taranaki Graben Complex and the Western Platform (Pilaar and Wakefield, 1984). The Tui3D seismic survey (the orange star) is situated offshore Taranaki Basin, New Zealand. After King et al. (1993), King and Thrasher (1996), Thrasher et al. (2002), and Hansen and Kamp (2006). (b) Stratigraphic column of the Taranaki Basin, New Zealand. The Moki Formation (the red rectangle) can be divided from the lower to the upper unit into the Moki B sands, Moki B shale, and Moki A sands (Engbers, 2002). The Moki A sands unit is the zone of interest in this research, and it is characterized by the base of slope turbidities and channel complexes (Engbers, 2002) trending northwest–southeast (Yagci, 2016). Picture after De Bock (1994).

sedimentation associated to deposition of bathyal claystones (Engbers, 2002), and it tends to thicken to the east and northeast (Bussell, 1994). The Moki A sands unit was deposited as a base of slope turbidite (Engbers, 2002), and it is characterized by major submarine meandering channel complexes (Bussell, 1994) trending northwest–southeast (Yagci, 2016). According to Bussell (1994), the Moki B sands have few channels, whereas the Moki A sands are incised by sinusoidal channel complexes, consistent with a progradation of the slope model. The channel complexes present in the Moki A sands unit are the geologic feature of interest in this study.

## Data set

The Tui3D seismic survey is located offshore Taranaki Basin on the southwest coast of the North Island, New Zealand (Figure 4a), and it was acquired by Veritas DGC Australia Pty. Ltd from 25 March 2003 to 10 May 2003 (Veritas DGC, 2003). The Tui3D seismic volume provided by New Zealand Overseas Petroleum Limited has a surface area of 350 $km^2$ with a streamer separation of 150 m and a source separation of 75 m and a $12.5 \times 12.5$ m bin size.

The Tui3D seismic volume data quality is good, but it was contaminated by the acquisition footprint. A phase shift of 180° was applied to the volume resulting in a zero-phase American polarity. In addition to the seismic volume, we use the Tui SW-2 well to validate our unsupervised seismic facies analysis.

### *Seismic attributes and analysis interval*

Seismic attributes are powerful tools that quantitatively measure properties such as continuity, morphology, and frequency, facilitating the identification of turbidites and channel complexes in this seismic data volume. Different attributes highlight different features of interest. Combining them using multiattribute analysis techniques provides a means to better understand the underlying geologic processes and to better characterize the reservoir.

Zhao et al. (2015) and Marfurt (2018) summarize some of the more commonly used multiattribute data integration tools, such as 3D corendering, PCA, and SOMs among other. In this paper, we evaluate the relatively new ICA multiattribute decomposition technique.

To apply the ICA algorithm to make a facies analysis and study the geomorphology of the turbiditic channel complexes in the Moki A sands Formation, several seismic attributes are used as input. The choice of these attributes is critical to obtain satisfactory results. Spectral components are sensitive to impedance and thickness variations and are thus good candidates for turbidite analysis. We hypothesize that applying ICA to spectral magnitude components will reduce the dimensionality of the data, reject noise, and extract the most valuable information components, thus accomplishing our goal of highlighting the turbiditic channels to study their internal architecture and facies distribution.

Spectral-decomposition analysis is a powerful technique for studying bed thickness, lateral changes in porosity, the presence of hydrocarbons (Sinha et al., 2005; Chopra and Marfurt, 2014), and the sequence stratigraphy and the deposition of a particular system (Marfurt and Kirlin, 2001). The method of choice in this study was the continuous wavelet transform (CWT) that decomposes the seismic volume into phase and magnitude components at different time-frequency samples, often improving the temporal and vertical resolution and allowing us to interpret geologic features at different scales. These frequency components are similar to applying a band-pass filter to the volume and represent its information at a particular frequency (Chopra and Marfurt, 2015, 2016).

Besides an appropriate choice of seismic attributes, another critical factor for multiattribute facies analysis techniques is the design of the analysis interval. The ideal analysis interval encloses only the target formation thereby avoiding mixing adjacent facies that have no geologic interest with the target turbidite facies and basin floor matrix. Fewer facies results in easier facies discrimination.

In this study, the Moki A sands unit consists of strong continuous reflectors incised by discontinuous reflectors with variable reflectivity (Figure 5). For this reason, picking a consistent horizon through the Moki A sands Formation is a challenging task. Instead, we

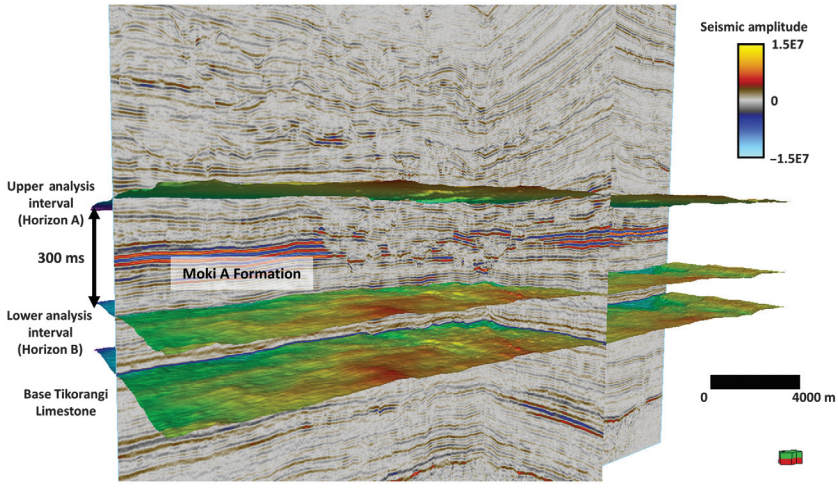


**Figure 5.** Analysis interval between horizon A and horizon B enclosing the Moki Formation. A strong continuous reflector associated with the Tikorangi Limestone was picked, and phantom horizons were created bracketing the Moki Formation. To completely enclose the channel complexes present in the Moki A sands Formation, the analysis interval brackets the Moki A sands Formation, the Moki B Shale, and parts of the Moki B sands and Upper Manganui. The analysis interval has a width of 300 ms.

Downloaded 07/31/19 to 68.97.115.26. Redistribution subject to SEG license or copyright; see Terms of Use at http://library.seg.org/

picked a horizon along the base of the Tikorangi Limestone, characterized by a strong continuous reflector and similar depositional trend as the Moki Formation, to create phantom horizons bracketing the top and bottom of the Moki A sands Formation resulting in an analysis interval of 300 ms. Although the ideal analysis interval should enclose only one target formation, to completely enclose the channel complexes present in the Moki A sands Formation, our 300 ms analysis interval brackets the Moki A sands Formation, the Moki B shale, and part of the Moki B sands and Upper Manganui Formations.

## Results

### *Seismic geomorphology and facies analysis using spectral magnitude components as input in the ICA*

To interpret the geomorphology and facies of the channel complexes present in the Moki A sands unit, each spectral magnitude component, independent component, and principal component volumes are flattened against the top analysis interval horizon (horizon A), which is equivalent to extracting a suite of phantom horizons parallel to horizon A (Figure 6).

Spectral magnitude components are often plotted against an RGB color scheme for their interpretation (Li and Lu, 2014; Li et al., 2018). If we plot different combinations of these spectral components along a phantom horizon A + 196 ms, we note that the combination of 25–35–45 Hz (Figure 7a) is similar to the combination of 40–50–60 Hz (Figure 7b), even though a small meandering channel (blue arrow) tends to be better resolved in the former. In contrast, the combination of 60–70–80 Hz (Figure 7c) is contaminated by the strong acquisition footprint (red rectangle), but it delineates thin beds inside the channels (yellow arrows). If we plot the 25–50–75 Hz (Figure 7d), we note that the infill of the channels tends to tune at the low frequencies while their flanks are more coherent at approximately 50 Hz; also, some thin beds tune at high frequencies of approximately 75 Hz. Analyzing the same combinations at horizon A + 248 ms (Figure 8), we still observe that the infill of the channels tends to tune at low frequencies, the flanks, internal thin beds, and acquisition footprint tune at higher frequencies.

Besides the redundant data existing in the spectral component analysis, selection of which combination better represents the turbiditic channels in the Moki A sands Formation can be cumbersome because there are many output components to choose from, requiring manually scrolling and analysis of each combination. The internal architecture of the channel complexes is poorly captured at 10, 15, and 20 Hz. For these reasons, in workflow 1 (Figure 9), we analyze the spectral magnitude components ranging from 25 to 80 Hz with intervals of 5 Hz in the PCA and ICA algorithms. Based on the retained variability criteria (Stanford, 2018), the algorithm automatically outputs four principal components, from which the independent components are computed because they represent 94.04% of the variability of the data (Figure 10a).

Workflow 1 reduces the 12D attribute space to a 4D mathematical space, in which the 12D vectors at each voxel are projected against the whitened eigenvectors and the results projected against the unmixing matrix **W**. Therefore, if we project the independent components against an RGB color scheme, voxels that are projected to similar colors can be considered as similar seismic facies.

Principal components are sorted based on the energy represented by their eigenvalues. Thus, the first principal component (PC1) is the strongest in these data and represents 63.52% of the variability (Figure 10a). In general, the complex seismic spectrum is the product of the spectrum of the seismic source and the spectrum of the geologic response, where the latter exhibits the effects of thin-bed tuning, reflection strength, attenuation, and scattering. To examine the spectral response of such geologic sources, it is common practice to first statistically flatten the unknown source spectrum. Such flattening is possible if the average lateral and vertical changes in reflectivity can be considered to be random and white over the lateral extent of the survey, and in this case, within a 1 s analysis window. For this reason,

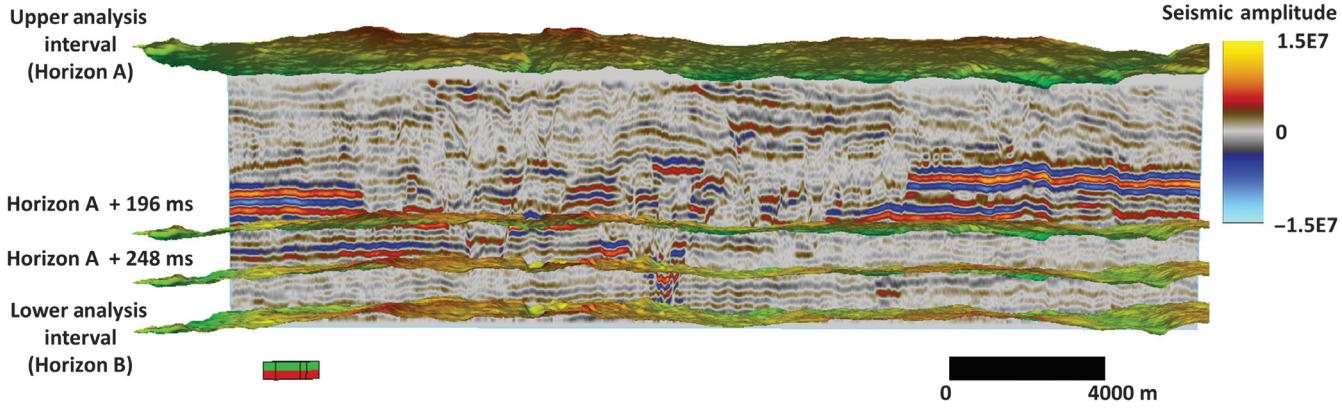


**Figure 6.** Spectral magnitude, independent, and principal components volumes are flattened against the top analysis interval horizon A. This procedure is similar that extracting them along phantom horizons within the analysis interval.



Downloaded 07/31/19 to 68.97.115.26. Redistribution subject to SEG license or copyright; see Terms of Use at http://library.seg.org/

the eigenspectrum that best represents the data (PCA1) is approximately flat (Figure 10b). Guo et al. (2009) observe that because the principal components reside in a mathematical space, where the spectral components are represented as orthogonal uncorrelated components, little physical significance can be assigned to these spectra. Moreover, under a non-Gaussian distribution, such as the Poisson distribution associated with the spectral magnitude components, PCA cannot recover the independent sources (Shlens, 2014), but rather it provides a different mixture of variabilities with a low physical meaning (Kim and Wu, 1999; Aires et al., 2000)

Unlike the principal components that are ordered by their statistical contribution to the final image, the order of the independent components is undefined because they were preprocessed to have unit variance, such that all four components represent similar energy (Figure 11a). For this reason, the interpreter evaluates the components subjectively, based on the relevance of the imaged geologic features. The noisiest energy is defined as IC4. Because the independent components reside in a space where the spectral components are represented as oblique projections obtained by maximizing the non-Gaussianity of the data to find the underlying independent sources (Hyvärinen, 2012), we hypothesize that the ICA spectrum has more physical significance that the PCA eigenspectrum. We evaluate this hypothesis in Figure 11b, which shows the ICA spectrum generated by plotting the columns of the whitened eigenvectors matrix by the unmixing matrix **W** where, similar to the PCA eigenspectrum, each column has a value associated with the frequencies ranging from 25 to 80 Hz.

Comparing the variability of the principal components (Figure 10a) with the energy of the independent components (Figure 11a), we observe that PCA tends to be dominated by PC1, whereas the independent components exhibit almost the same energy and thus are equally important. To avoid a subjective comparison between PCA and ICA, in Figures 12, 13, 14, and 15, we first examine each of the principal components sorted by their energy (measured by the corresponding eigenvalues), and we compared them with the results obtained analyzing each of the independent components seen in Figures 16, 17, 18, and 19, which are sorted visually, using the delineation of large- and small-scale geologic features as the sorting criterion.

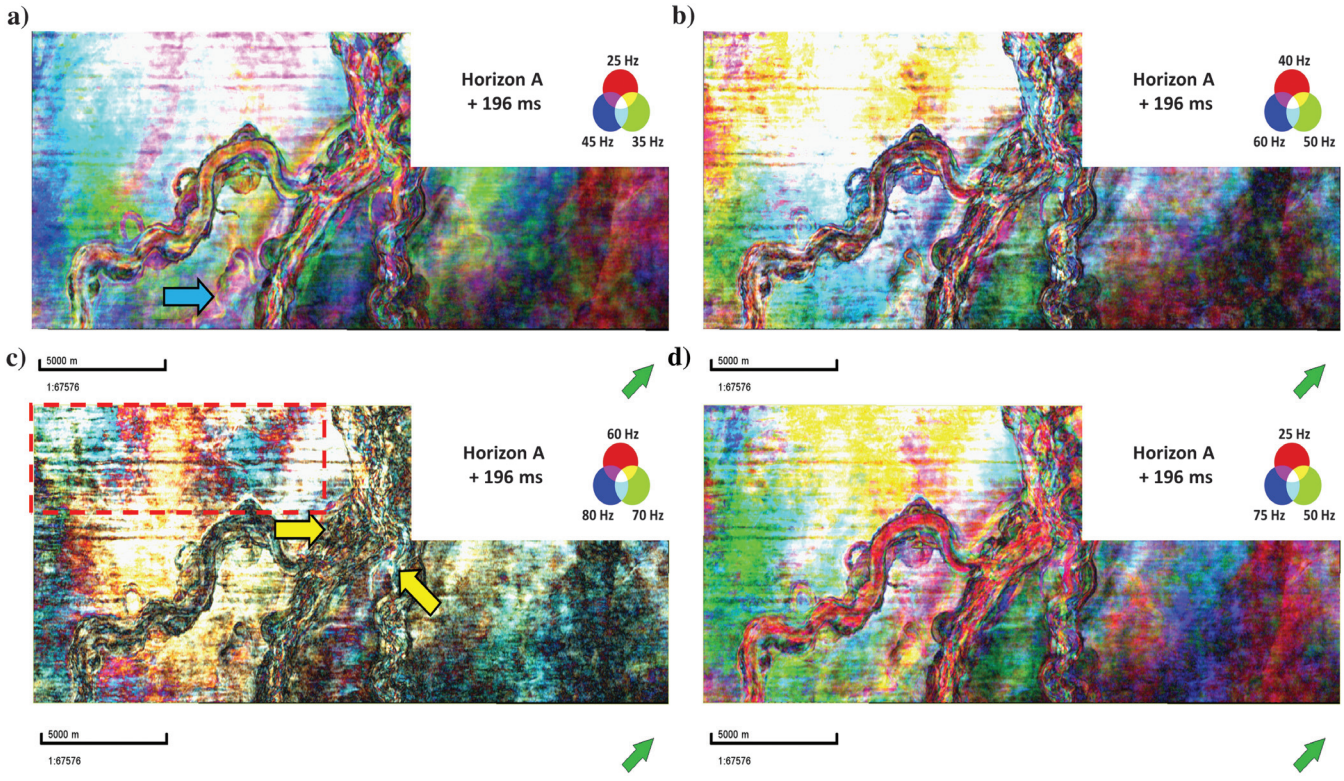


**Figure 7.** Spectral magnitude components plotted against an RGB color scheme along a phantom horizon A + 196 ms. (a) Combination of 25–35–45 Hz spectral magnitude components showing the channel complexes present in the Moki A sands Formation. (b) The combination of 40–50–60 Hz also shows the channel complexes; however, the small-scale abandoned meandering channel (the blue arrow) is better resolved in the combination of 25–35–45 Hz. (c) Combination of 60–70–80 Hz. At higher frequencies, the picture is contaminated by acquisition footprint (the red rectangle). Internal architecture of the channel is still delineated (the yellow arrows). (d) Combination of the 25–50–-75 Hz. Infill of the channels predominantly tunes at lower frequencies than their flanks (approximately 50 Hz). Thin beds inside the channels tune at approximately 75 Hz.



Downloaded 07/31/19 to 68.97.115.26. Redistribution subject to SEG license or copyright; see Terms of Use at http://library.seg.org/

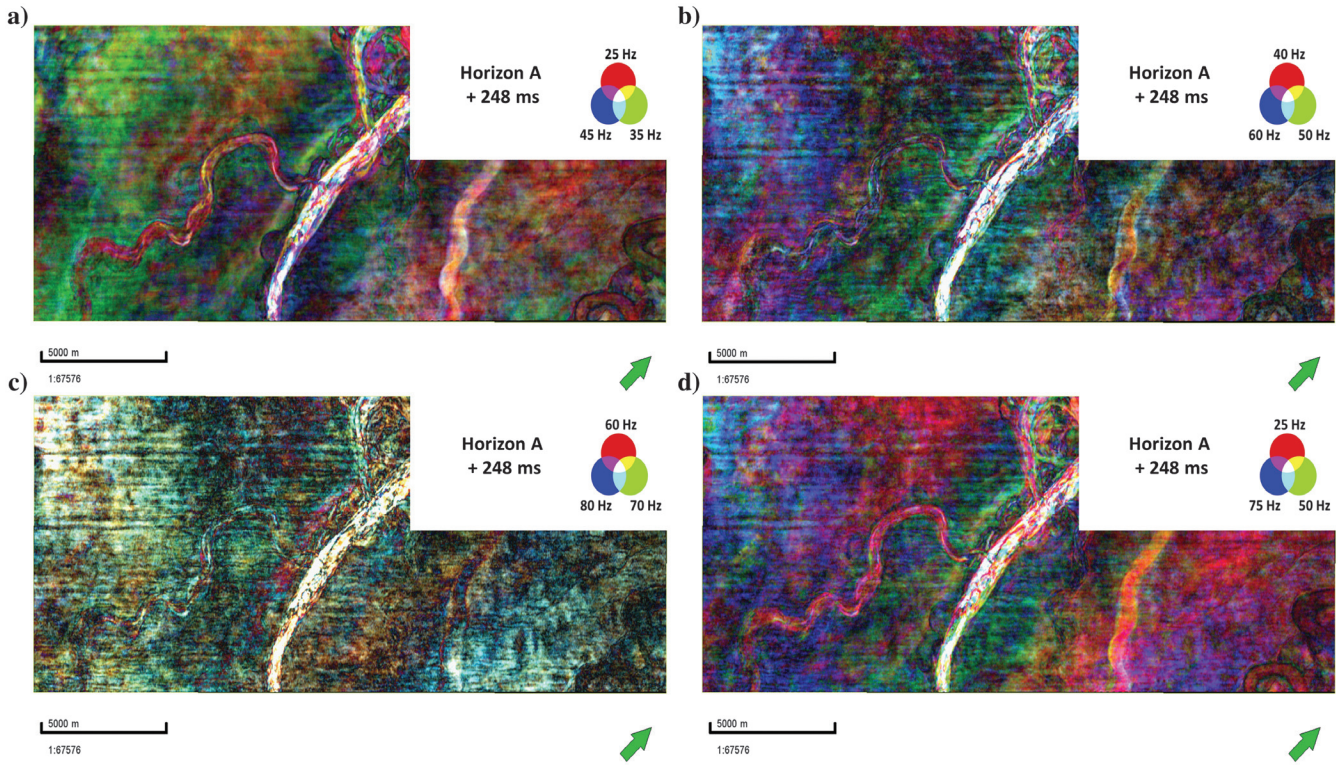


**Figure 8.** Spectral magnitude components plotted against an RGB color scheme along a phantom horizon A + 248 ms. Analyzing the same combinations as in Figure 7, the infill of the channels still tunes at lower frequencies, whereas the flanks, internal thin beds, and acquisition footprint tune at higher frequencies.

**Figure 9.** Proposed workflow to highlight and study the internal architecture of the channel complexes present in the Moki A sands Formation. We use spectral magnitude components ranging from 25 to 80 Hz with intervals of 5 Hz to analyze the stratigraphy and depositional system of the target area. ICA attempts to extract stronger correlated patterns in the data (geology and acquisition footprint), with random uncorrelated noise remaining in the residual. The independent components are sorted by visual inspection using geologic insight. For PCA and ICA, we corender the three most useful components using RGB blending.

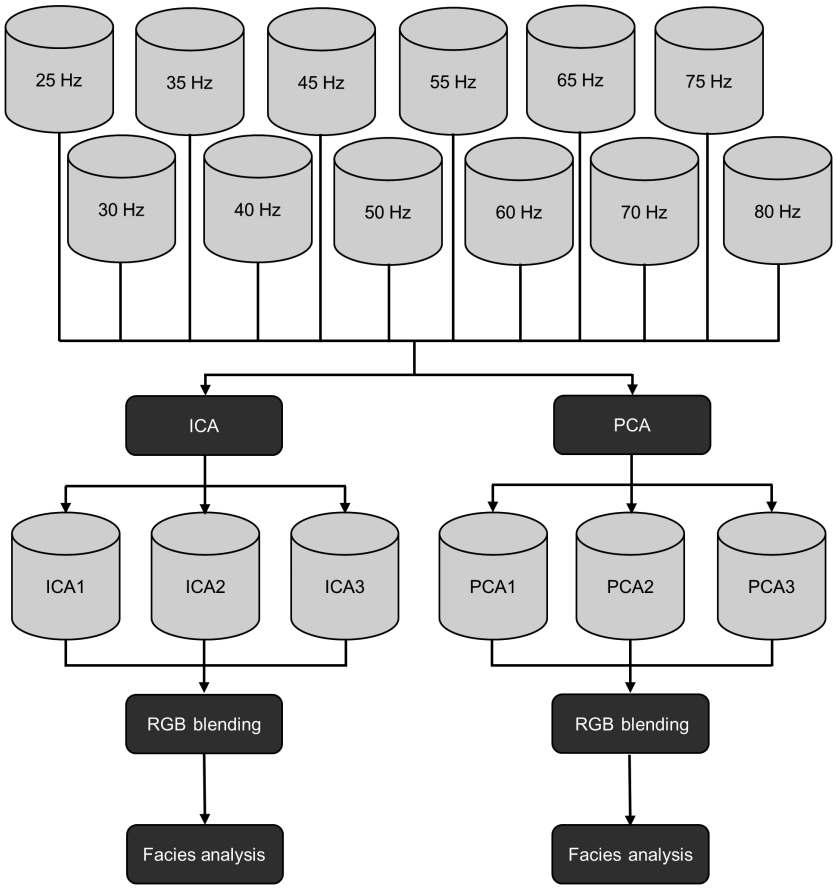


Downloaded 07/31/19 to 68.97.115.26. Redistribution subject to SEG license or copyright; see Terms of Use at http://library.seg.org/

Downloaded 07/31/19 to 68.97.115.26. Redistribution subject to SEG license or copyright; see Terms of Use at http://library.seg.org/

### *Geologic features seen on the principal components*

Let us first examine principal component 1 (PC1) at horizon A + 196 ms (Figure 12a) in which the numbering denotes the different architectural elements and is not associated with the time of deposition of the channel complexes. Note the confluence of two leveed meandering tributary channels with moderate sinuosity as well as a tabular-shaped channel with an architecture similar to a braided channel (green arrows). The merging of these three late lowstand turbidite channel infill systems forms a major turbidite channel toward the northwest of the study area. In addition, PC1 is characterized by a strong acquisition footprint (red rectangle) and random noise. Small-scale geologic features such as oxbow 1, oxbow 2, oxbow 3 (orange arrows), and a small abandoned meandering channel (blue arrow) are visible but are difficult to delineate using PC1.

Along horizon A + 248 ms (Figure 12b), PC1 still exhibits a strong acquisition footprint (the red rectangle) and random noise. Although we can delineate the tabular shape channel and its bifurcation into two distributary channels toward the northwest, the leveed meandering channels (the green arrows) and the small-scale oxbow 3 (the orange arrow) are difficult to interpret.

PC2 at horizon A + 196 ms (Figure 13a) is somewhat similar to PC1, exhibiting strong acquisition footprint (the red rectangle) and random noise. Although we can still observe the larger scale geologic features such as the leveed meandering channel and the tabular shape channel (the green arrows), the smaller scale geologic features such as oxbows (the orange arrows) and the small abandoned channel (the blue arrow) are less apparent than on PC1.

Although PC2 along horizon A + 248 ms (Figure 13b) still exhibits acquisition footprint (the red rectangle) and random noise, the image is smoother and less noisy than PC1. The tabular-shaped channel and its distributary channels bifurcating toward the northwest of the study area and the meandering channels (the green arrows) are similarly resolvable than in PC1, although meandering channels 1 and 3 look easier to interpret in PC2. The small-scale oxbow 3 (the orange arrow) is difficult to delineate using PC2.

Figure 14a shows principal component 3 (PC3) along horizon A + 196 ms. The leveed meandering channels, the tabular-shaped and the subsequent merged main channels (the green arrows), together with the small-scale oxbows (the orange arrows) images are similar to those in PC1 and PC2. However, the small abandoned channel (the blue arrow) that was not completely delineated in PC1 and PC2 is now visible in PC3.

Along horizon A + 248 ms (Figure 14b), PC3 exhibits less acquisition footprint (the red rectangle) and random noise than previous principal components. Moreover, the leveed meandering tributary channels 1, 2, 3, and 4 have better resolution in PC3 compared with PC1 and PC2, whereas the tabular-shaped channel and its

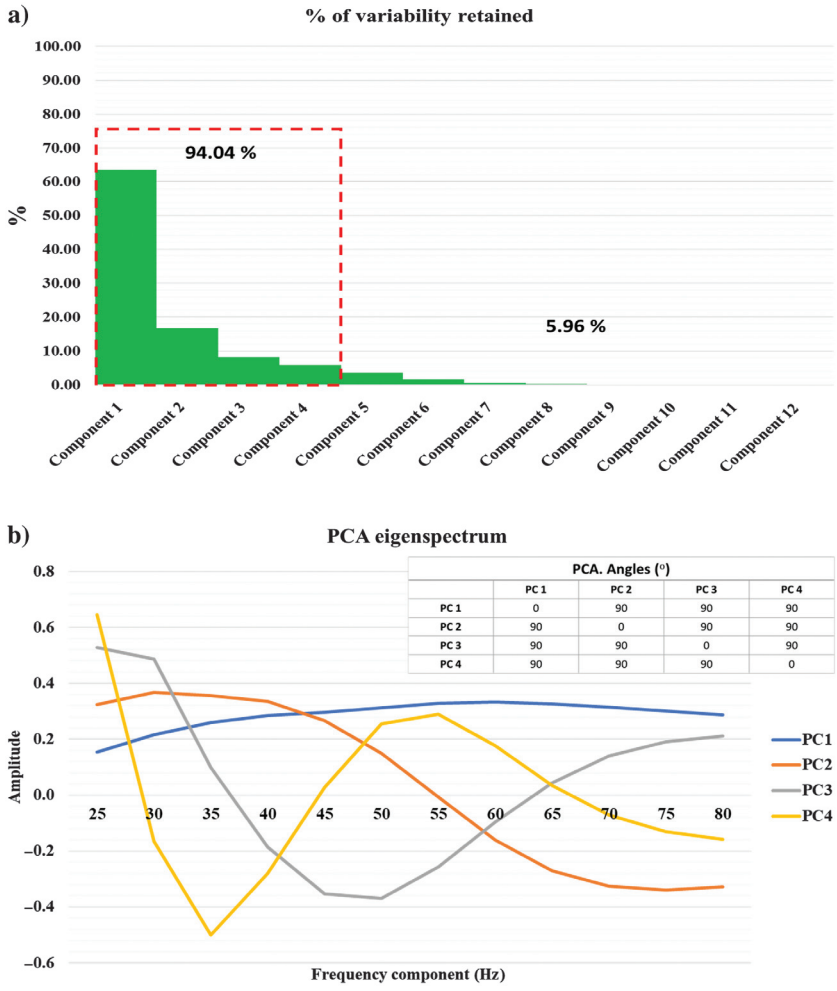


**Figure 10.** Variability retained. (a) Based on the percentage of variability retained (Stanford, 2018), the algorithm automatically outputs four components during the PCA whitening preprocessing step that represent 94.04% of the variability of the data, from these components the independent components are computed. Also, PC1 is the strongest and represent 63.52% of the variability and (b) PCA eigenspectrum. PC1 is characterized by a flat spectrum because the spectral magnitude components were spectrally balanced during the CWT spectral decomposition. Because principal components reside in a mathematical space and under a non-Gaussian distribution such as the Poisson distribution associated with the spectral magnitude components, little physical significance can be assigned to these spectra because PCA recovers a new mixture of variabilities (Kim and Wu, 1999; Aires et al. 2000; Guo et al., 2009; Shlens, 2014).

bifurcations (distributary channels 1 and 2) look equally resolvable.

Finally, analyzing principal component 4 (PC4) along horizon A + 196 ms (Figure 15a) and horizon A + 248 ms (Figure 15b), we note that it still exhibits the acquisition footprint (red rectangle) and random noise seen in PC1, PC2, and PC3. Nevertheless, the edges and internal architecture of the geologic deepwater elements analyzed before are not as well-delineated as in the other principal components (PC1, PC2, and PC3), although the edges of the leveed meandering channel 1 at horizon A + 248 are better delineated.

### *Geologic features seen on the independent components*

Figure 16a of independent component 1 (IC1) along horizon A + 196 ms shows the confluence of two leveed meandering channels with the tabular-shaped channel forming a major turbidite channel toward the northwest (the green arrows). However, we note that IC1 presents better footprint suppression (the red rectangle) and a smoother, less noisy picture than all the principal components. Moreover, the large-scale channels (the green arrows) and small-scale features such as oxbow 1, oxbow 2, oxbow 3 (the orange arrows) and the small abandoned meandering channel (the blue arrow) are better delineated and internally resolvable using IC1.

Figure 16b of IC1 along horizon A + 248 ms shows better resolution, less random noise, and better footprint suppression (red rectangle) than all the principal components. Furthermore, while the leveed meandering channels (green arrows) are difficult to delineate using the principal components, these are well-resolved in IC1. In addition, the tabular-shaped channel that bifurcates into two distributary channels toward the northwest is being better delineated and internally resolved using IC1. The small-scale oxbow 3 (orange arrow) is also better resolved by IC1.

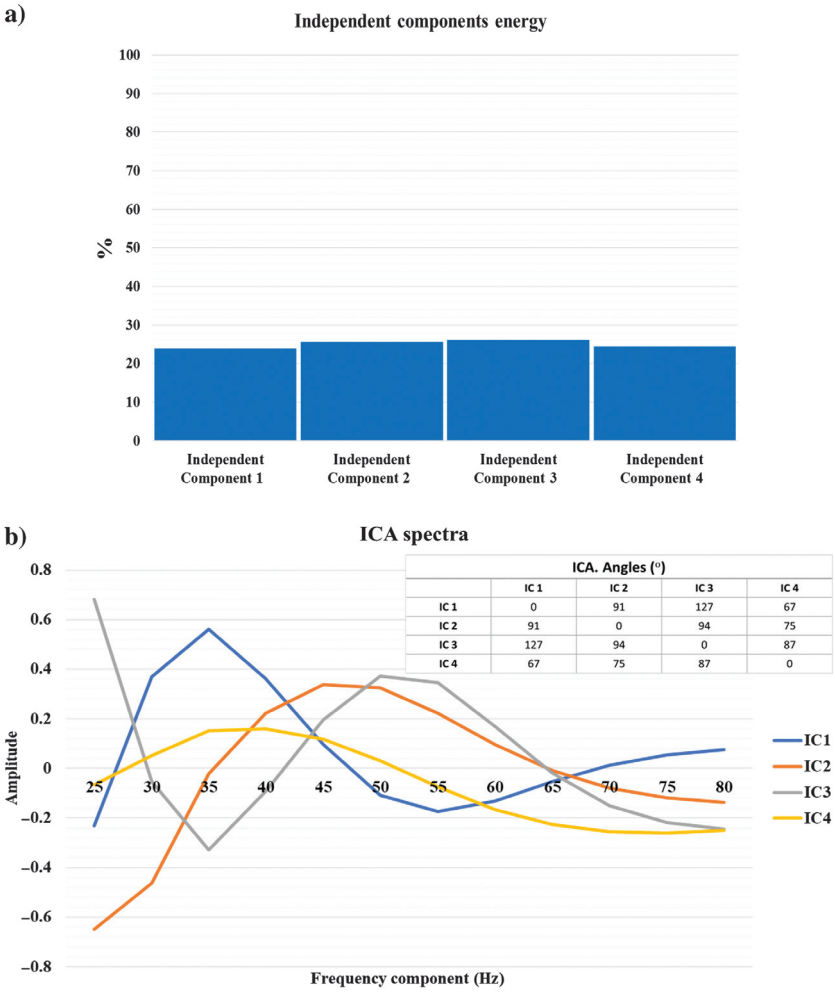


**Figure 11.** The ICA energy. (a) Independent components exhibit similar energy, and this is not clearly correlated to geology, thus independent components are sorted based on visual inspection, seeking for better resolution of large- and small-scale geologic features and (b) ICA spectra. ICA, in which projections are not necessarily orthogonal, find the underlying geologic sources by maximizing the non-Gaussianity of the data (Hyvärinen, 2012); thus, we believe that the ICA spectrum has more physical meaning than the PCA eigenspectrum.

Figure 17a of independent component 2 (IC2) along horizon A + 196 ms appears to be smoother, less noisy with better footprint suppression (the red rectangle) than all the principal components. IC2 also better shows the large-scale geologic features such as the leveed meandering channels and the tabular-shaped channel (the green arrows), as well as the small-scale geologic features such as oxbows (the orange arrows) and the small abandoned channel (the blue arrow) than any of the principal component images.

Figure 17b of IC2 along horizon A + 248 ms provides better delineation of the large-scale leveed meandering tributary channels (the green arrows) and the small-scale oxbow 3 (the orange arrow) than any of the principal component images. Like IC1, IC2 exhibits a smaller acquisition footprint (the red rectangle) and less random noise than the principal components.

Figure 18a of IC3 along horizon A + 196 ms still exhibits a smaller footprint (the red rectangle) and random noise than the principal components (the red rectangle), even though it has a bigger footprint and looks noisier than IC1 and IC2. The leveed meandering channels, the tabular-shaped and the subsequent merged main channels (the green arrows), together with the small-scale oxbows (the orange arrows) are better delineated using IC3 than in the principal components. However, the small abandoned channel (the blue

Downloaded 07/31/19 to 68.97.115.26. Redistribution subject to SEG license or copyright; see Terms of Use at http://library.seg.org/

arrow) that was not completely delineated in PC1 and PC2 but, was visible in PC3, is barely resolved in IC3.

Figure 18b of IC3 along horizon A + 248 ms shows the leveed meandering tributary channels 1 and 2 are still better delineated in IC3 compared with PC1, PC2, and

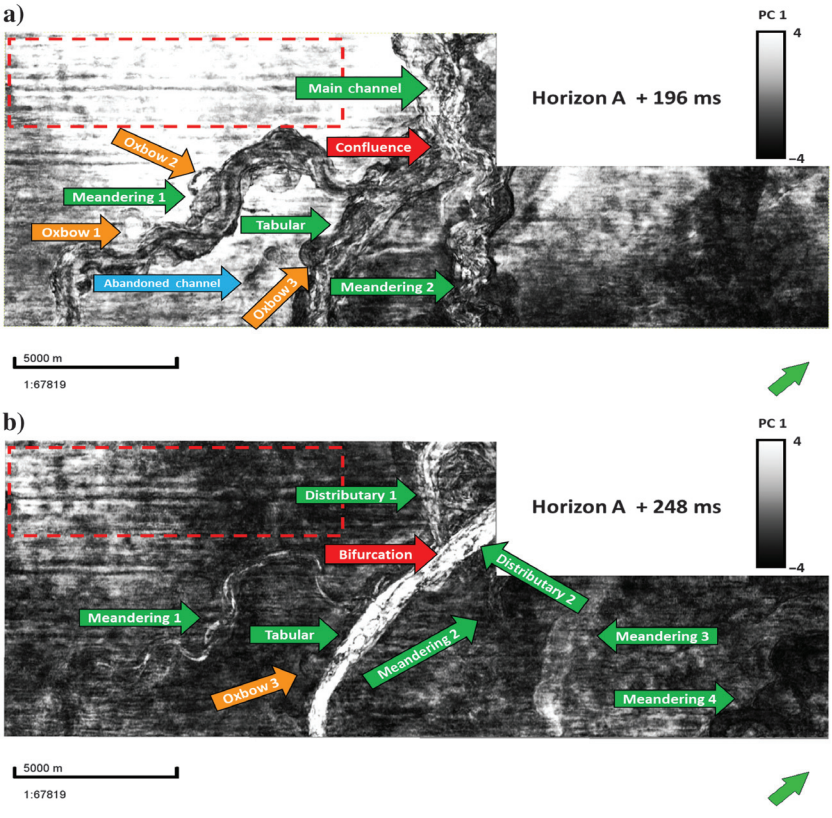


**Figure 12.** Principal component 1 (PC1). (a) Along horizon A + 196 ms, we note the confluence of two leveed meandering tributary channels and a tabular-shaped channel into major turbidite channel toward the northwest (the green arrows). Also, we observe strong acquisition footprint (the red rectangle) and random noise. Moreover, small-scale geologic features (the orange arrows) and a small abandoned meandering channel (the blue arrow) are difficult to delineate. (b) PC1 at horizon A + 248 ms. PC1 is still characterized by random noise and strong acquisition footprint (the red rectangle). The large-scale leveed meandering channels (the green arrows) and the small-scale oxbow 3 (the orange arrow) are difficult to interpret. Please note that the numbering is used to identify the different architectural elements, and it is not associated with time of deposition of the channel complexes.

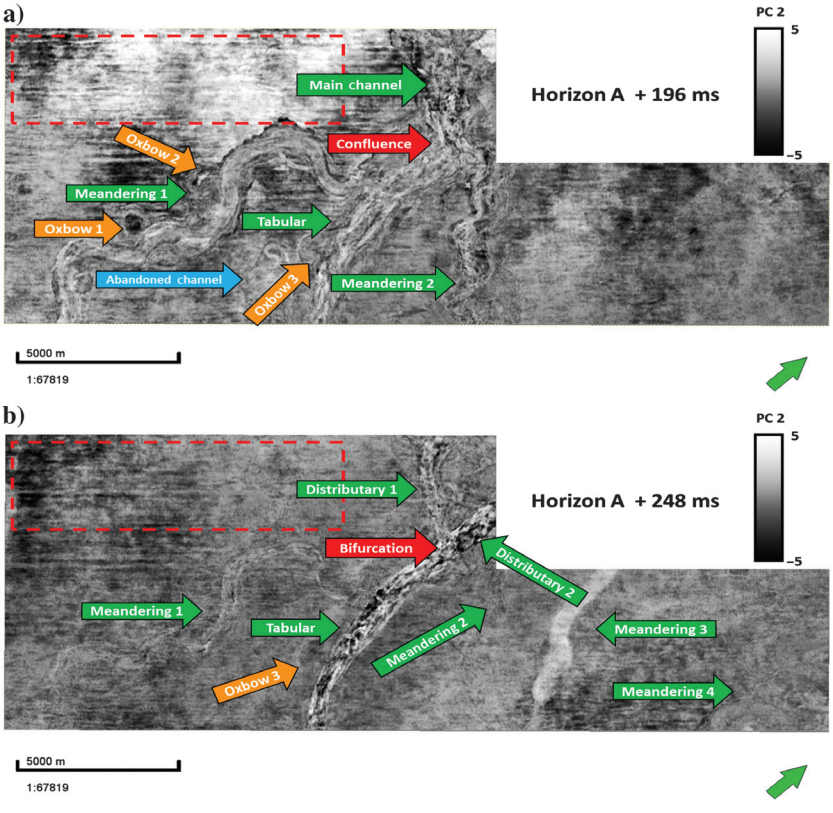


**Figure 13.** Principal component 2 (PC2). (a) Similar to PC1, PC2 along horizon A + 196 ms shows a strong acquisition footprint (the red rectangle) and random noise. Large-scale geologic features such as the tabular-shaped and the leveed meandering channels (the green arrows) are possible to delineate. However, small-scale geologic features such as the small abandoned channel (the blue arrow) and oxbows (the orange arrows) have lower resolution in PC2 compared to PC1. (b) Along horizon A + 248 ms, PC2 looks smoother than PC1, although we observe random noise and acquisition footprint (the red rectangle). The meandering channels 1 and 2 present better resolution in PC2 than PC1, whereas the tabular-shaped channel and its distributary channels toward the northwest of the study have similar resolution on both principal components. The small-scale oxbow (the orange arrow) is difficult to interpret using PC2.

Downloaded 07/31/19 to 68.97.115.26. Redistribution subject to SEG license or copyright; see Terms of Use at http://library.seg.org/

PC3. In addition, IC3 shows similar resolution than PC2, PC3, and PC4 when interpreting the meandering channel 4 and better resolution than PC1 and PC4 when analyzing the meandering channel 3. The small-scale oxbow 3 (the orange arrow) is delineated using IC3, but it is clearer using PC3.

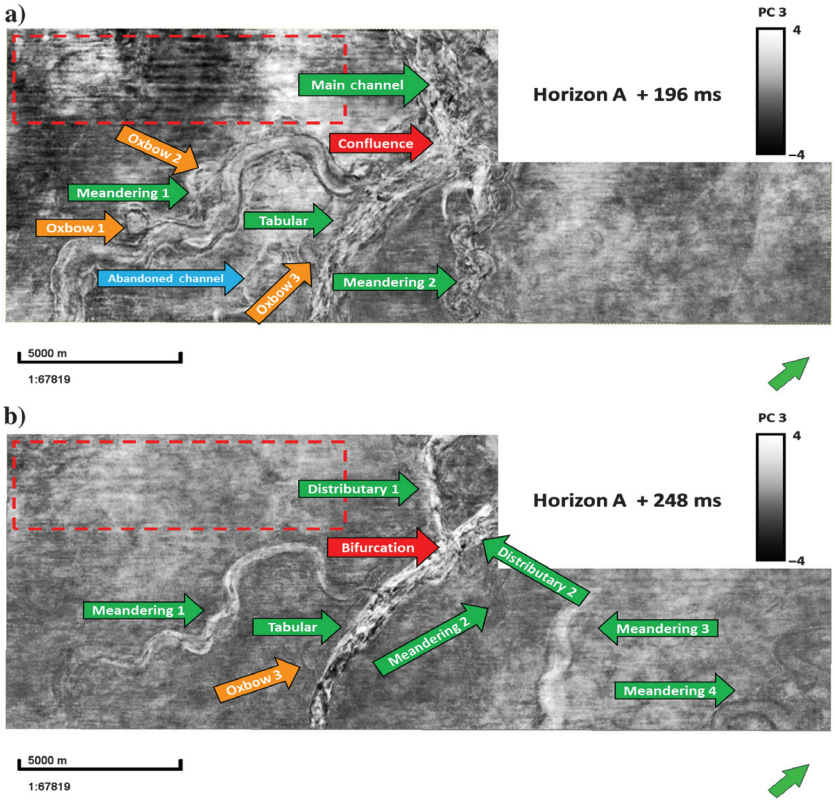


**Figure 14.** Principal component 3 (PC3). (a) At horizon A + 196 ms, the large-scale (the green arrows) and small-scale (the orange arrows) geologic features are similarly interpretable than in PC1 and PC2. Nevertheless, the small abandoned channel (the blue arrow) is better resolved using PC3. (b) PCA 3 along horizon A + 248 ms exhibits a smaller acquisition footprint (the red rectangle) and less random noise than previous principal components. Although the tabular-shaped channel and distributary channels 1 and 2 look equally resolved than in PC1 and PC2, the meandering channels 1, 2, 3, and 4 have better resolution in PC3. Similar to Figures 12 and 13, numbering is used to identify the different architectural elements, and it is not associated with time of deposition of the channel complexes.

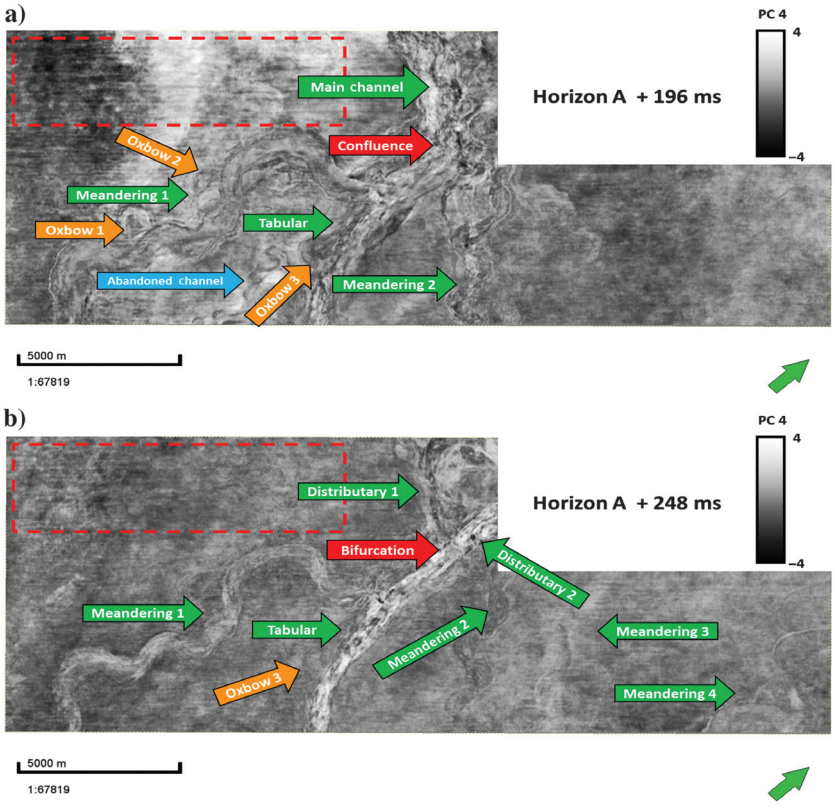


**Figure 15.** Principal component 4 (PC4). (a) Along horizon A + 196, PC4 exhibits similar random noise and acquisition footprint (the red rectangle) than previous principal components. However, the internal architecture and edges of the geologic deepwater elements present less resolution than in PC1, PC2, and PC3. (b) PC4 at horizon A + 248 ms is still characterized by acquisition footprint (the red rectangle) and random. In addition, although the edges and internal architecture of the deepwater elements are better delineated in the previous principal components, the edges of the leveed meandering channel 1 are better resolved using PC4 along horizon A + 248 ms.

Downloaded 07/31/19 to 68.97.115.26. Redistribution subject to SEG license or copyright; see Terms of Use at http://library.seg.org/

Figure 19a of IC4 at horizon A + 196 ms and Figure 19b along horizon A + 248 ms are contaminated by strong acquisition footprint and random noise. The architectural elements of IC4 are poorly delineated when compared with IC1, IC2, and IC3. This observation is consistent with the objective of ICA, which seeks to

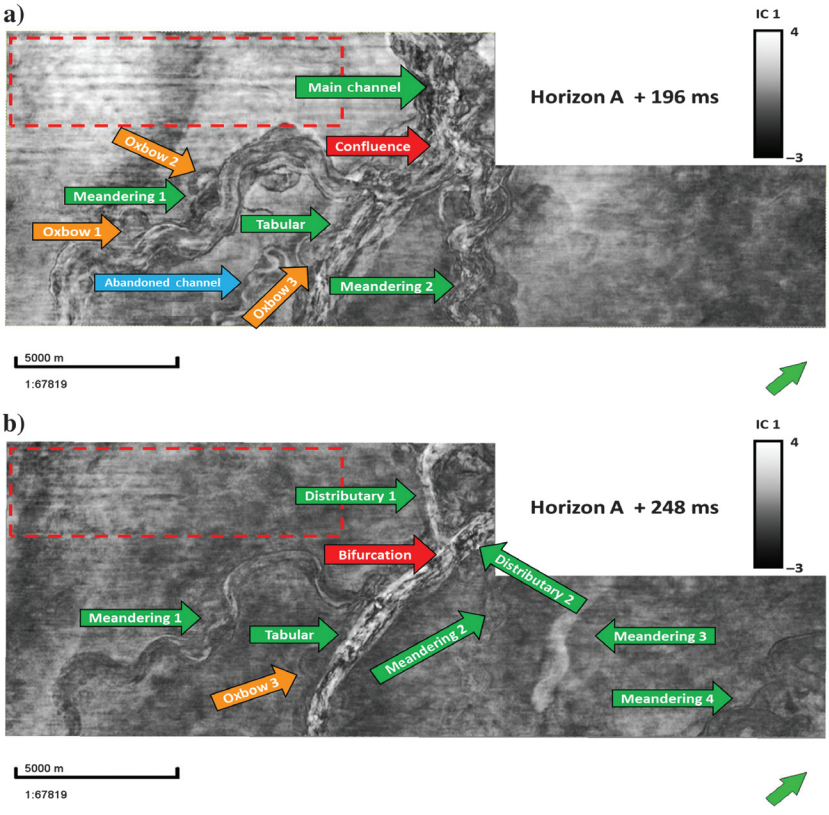


**Figure 16.** Independent component 1 (IC1). (a) At horizon A + 196 ms, IC1 shows better footprint suppression (the red rectangle) and a smoother, less noisy behavior than all the principal components. Furthermore, the large-scale (the green arrows) and small-scale oxbows (the orange arrow) and abandoned meandering channel (the blue arrow) are better internally resolved and delineated using IC1. (b) IC1 along horizon A + 248 ms still exhibits better resolution, less random noise, and a smaller acquisition footprint (the red rectangle) than all of the principal components. Moreover, the leveed meandering channels (the green arrows) and the small-scale oxbow 3 (the orange arrow) have better resolution in IC1 than in all principal components. In addition, the tabular shape channel and its distributary channels are better delineated and internally resolved. Similar to previous figures, numbering is used to identify the different architectural elements, and it is not associated with time of deposition of the channel complexes.

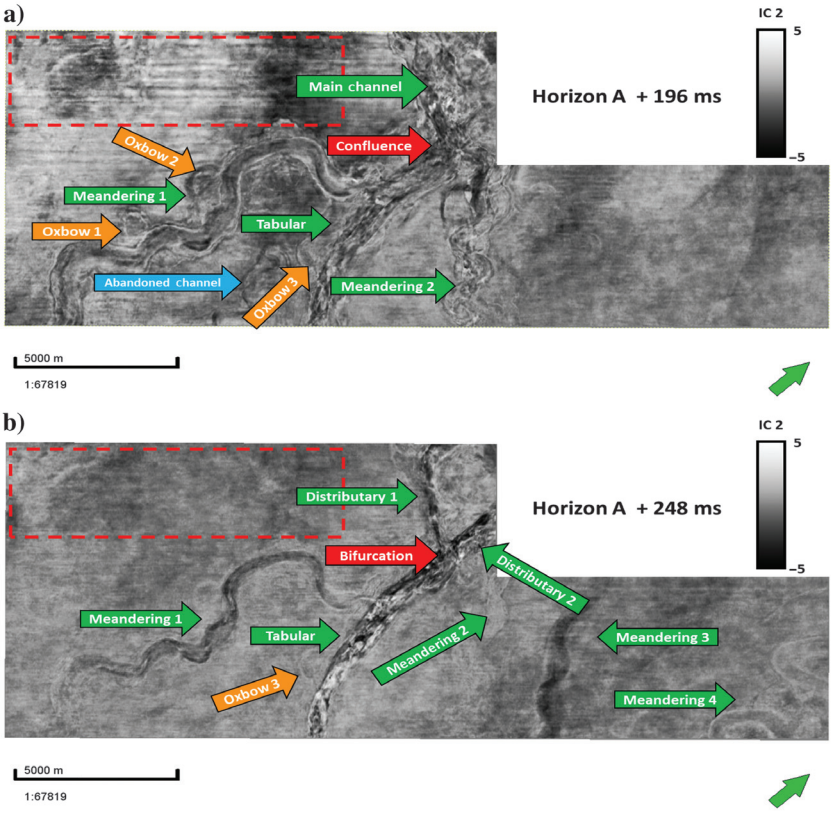


**Figure 17.** Independent component 2 (IC2). (a) Along horizon A + 196 ms, IC2 is still characterized by a smoother, less noisy behavior, and better footprint suppression (the red rectangle) than all the principal components. Furthermore, IC2 better exhibits the large-scale (the green arrows) and small-scale geologic features such as oxbows (the orange arrows) and the small abandoned channel (the blue arrow) than using PCA. (b) IC2 along horizon A + 248 ms shows a smaller acquisition footprint (the red rectangle) and better resolution of the large-scale (the green arrows) and the small-scale (the orange arrow) geologic features than the principal components.

Downloaded 07/31/19 to 68.97.115.26. Redistribution subject to SEG license or copyright; see Terms of Use at http://library.seg.org/

better separate alternative patterns or independent sources (e.g., the geologic features seen in IC1, IC2, and IC3 and the noise pattern seen in IC4). Moreover, because PCA sorts the data into orthogonal components based on higher variability, it tends to mix the geologic features of interest with noise (PC1, PC2, PC3, and PC4).

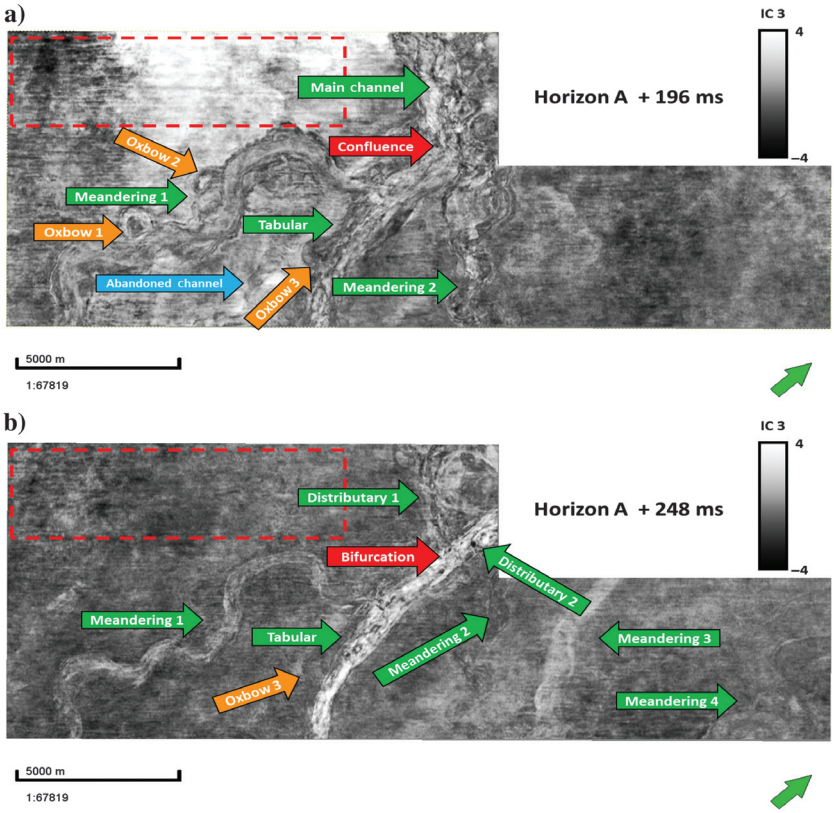


**Figure 18.** Independent component 3 (IC3). (a) IC3 at horizon A + 196 ms shows a smaller acquisition footprint (the red rectangle) and less random noise than the principal components, although it has a larger footprint and more random noise than IC1 and IC2. Moreover, the large-scale geologic features (the green arrows) and small-scale oxbows (the orange arrows) are better delineated than in PCA. However, the small abandoned channel (the blue arrow) that was not completely delineated using PC1 and PC2, but was resolvable in PC3, is barely delineated in IC3. (b) Along horizon A + 248 ms, IC3 shows similar resolution than PC2, PC3, and PC4 when delineating the meandering channel 4. However, IC3 has greater resolution than PC1, PC2, PC3 and PC1 and PC4, when interpreting the leveed meandering tributary channels 1 and 2 and the meandering channel 3, respectively. The small-scale oxbow 3 (the orange arrow) is possible to interpret using IC3, but it looks better highlighted using PC3.

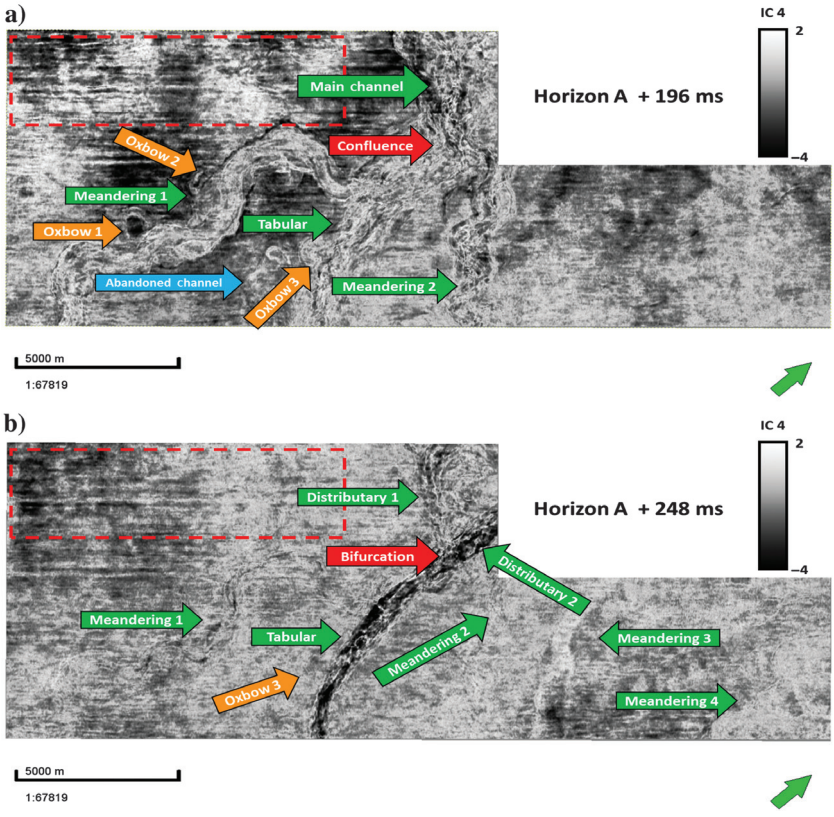


**Figure 19.** Independent component 4 (IC4). Along horizon A + 196 ms, IC4 is characterized by strong acquisition footprint (the red rectangle) and random noise. Architectural elements are difficult to delineate. (b) At horizon A + 248 ms, IC4 is still contaminated by strong acquisition footprint (the red rectangle) and random noise. Large- and small-scale geologic features are difficult to interpret. We hypothesize that because ICA looks for independence in the multivariate data, it provides better separation between geologic features (IC1, IC2, and IC3) and noise signal (IC4) than PCA, which, sorting the data using orthogonal components based on higher variability, tends to mix geologic features of interest with noise. Also, the independent components exhibit better resolution of large-scale and smaller scale geologic features than PCA, thus providing a means of making a better seismic interpretation.

Downloaded 07/31/19 to 68.97.115.26. Redistribution subject to SEG license or copyright; see Terms of Use at http://library.seg.org/

To accomplish the goal of making an unsupervised seismic facies analysis, we plot the independent components IC1, IC2, and IC3 that represent valuable geologic information against an RGB color scheme. By construction, similar seismic facies will appear as similar colors. In addition, we compare the ICA RGB blending with the PCA RGB blending using PC1, PC2, and PC3 in which 88.29% of the variability is retained.

In Figure 20, we note that the RGB blending using independent components at horizon A + 196 ms (Figure 20b) provides better resolution of geologic features than the RGB blending of principal components (Figure 20a). As in the individual components, the leveed meandering channels, the tabular-shaped main channels (green arrows) as well as the small-scale geologic features such as the older abandoned channel and the oxbows are better delineated using ICA. We also notice that the ICA RGB blending provides better contrast between the distinct seismic facies. Although the axis and off-axis of the leveed meandering channel (Posamentier and Kolla, 2003; McHargue et al., 2011; Fildani et al., 2013; Hubbard et al., 2014) are characterized by similar greenish colors in PCA RGB blending, they are characterized in the ICA RGB blending by a purple color for the axial deposition of the leveed meandering channels and a green color associated with the off-axis to marginal deposition. Moreover, we note that similar to a braided channel, the tabular-shaped tributary channel has a more variable internal architecture with predominantly purple seismic facies mixed with green and some blue seismic facies. In addition, the oxbows present different infill patterns. Oxbow 1 is filled by a blue, oxbow 2 by a purple, and oxbow 3 by a green seismic facies. Finally, the small abandoned channel, which is poorly captured in the PCA RGB image, is characterized by a purple seismic facies.

At horizon A + 248 ms (Figure 21), the leveed meandering channels 1 and 2 are much better delineated using ICA RGB blending (Figure 21b) than PCA RGB blending (Figure 21a). The leveed meandering channel 1 is characterized predominantly by purple seismic facies intercalated with some bluish seismic facies, whereas the leveed meandering channel 2 appears as a green seismic facies. At horizon A + 196 ms, the tabular-shaped channel internal architecture is highly variable with a mix of different seismic facies; this variability is better captured using ICA. The distributary channel 1 is characterized by a predominant purple seismic facies, whereas now the distributary channel 2 looks like a prolongation of the tabular channel because they have the same variable internal architecture. The meandering channel 3 is characterized by a purple seismic facies, whereas oxbow 3 and meandering channel 4 are characterized by a green infill.

In terms of random noise and footprint, ICA RGB blending (Figures 20b and 21b) provides a smoother

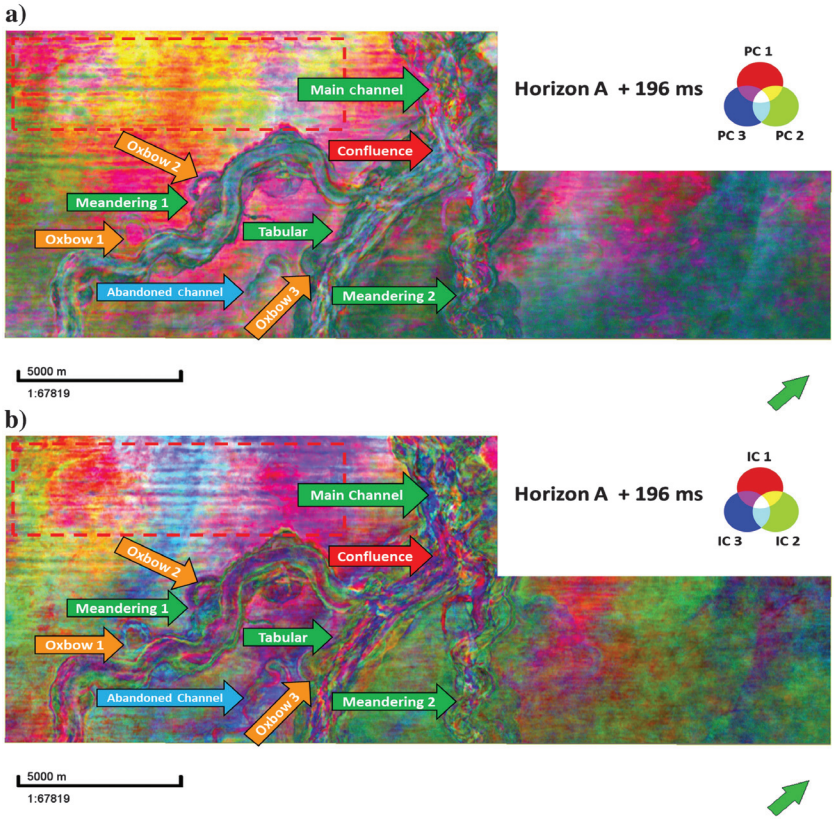


**Figure 20.** RGB blending of PC1, PC2, and PC3 versus RGB blending of IC1, IC2, and IC3 at phantom horizon A + 196 ms, in which similar colors can be interpreted as similar seismic facies. (a) From PCA RGB blending, it is possible to analyze the large-scale geologic features (the green arrows), and the small-scale oxbows (the orange arrows), but the small abandoned channel (the blue arrow) is only partially delineated. PCA RGB blending is contaminated by the acquisition footprint (the red rectangle). Axis and off-axis seismic facies are characterized by similar greenish colors. (b) From ICA RGB blending, the large-scale (the green arrows) and small-scale geologic features such as oxbows (the orange arrows) and the small abandoned channel (the blue arrow) are better delineated than in PCA RGB blending. In addition, the former presents a smaller acquisition footprint (the red rectangle) and less random noise than the latter. ICA RGB blending also provides a better contrast between different seismic facies; e.g., the axis of the channel is characterized with a purple seismic facies, whereas the off-axis of the channel is associated with a green seismic facies. In addition, the tabular-shaped channel is characterized by a more variable internal architecture with predominantly purple seismic facies mixed with blue and green seismic facies. Finally, the oxbows' infill varies from purple to blue and green facies, and the small abandoned channel is associated with the purple seismic facies.

Downloaded 07/31/19 to 68.97.115.26. Redistribution subject to SEG license or copyright; see Terms of Use at http://library.seg.org/

picture with remarkably less footprint than PCA RGB blending (Figures 20a and 21a). Even though the acquisition footprint in ICA RGB blending increases at horizon A + 196 ms, we hypothesize that it is associated with independent component 3 (IC3).

ICA shows better results than PCA in terms of delineating deepwater architectural elements of interest, reduces noise, and improve the contrast between different seismic facies. However, neither of these techniques can be used to predict thickness or porosity because the independent and principal components project the data onto a mathematical space. To study reflector thickness, we must use the original or reconstructed spectral components (Guo et al., 2009; Honorio et al., 2014).

### *Geologic interpretation of seismic facies using ICA RGB blending*

Following McHargue et al. (2011), channels associated with turbiditic deposits are a product of multiple waxing and waning flows. During a waxing cycle, high-energy turbiditic flows produce erosion forming a channel conduit. In a waning cycle, turbiditic flows become less energetic, thus allowing filling of the channel conduit.

Deposition in deepwater channels can be divided into axis, off-axis, and margin turbiditic facies (Figure 22). In most cases, the axis represents the thickest part of the channel and is characterized by deposition of thick-bedded amalgamated sandstone facies. In contrast, off-axis to marginal deposition is associated with interbedded sandstone and mudstone facies, also known as heterolytic facies, implying a lower concentration of net sand compared with axis facies (McHargue et al., 2011; Fildani et al., 2013; Hubbard et al., 2014).

Although the internal architecture of the channels present in the Moki A sands Formation is highly variable and complex, based on principles of geomorphology and following the model of deposition of turbiditic facies (McHargue et al., 2011; Fildani et al., 2013; Hubbard et al., 2014) and cut-and-fill architecture (Posamentier and Kolla, 2003) in channel complexes, we generate several vertical sections of seismic amplitude through the channels complexes, to correlate the different seismic facies obtained from the ICA RGB blending analysis with axis, off-axis, and margin deposition and lateral and upward migration of facies.

In Figure 23a, we generated a vertical section AA′ through the straight tabular-shaped channel that contains a more variable internal architecture of the seismic facies with predominantly purple seismic facies mixed with some green and blue facies. We hypothesize that this channel complex was developed as a deep cut associated with high-energy turbiditic flows in which, during a waning cycle, weakly unconfined channels migrated inside the channel conduit. According to McHargue et al. (2011), these weakly unconfined channels are characterized by a tabular shape and similar architecture to braided channels with predominant

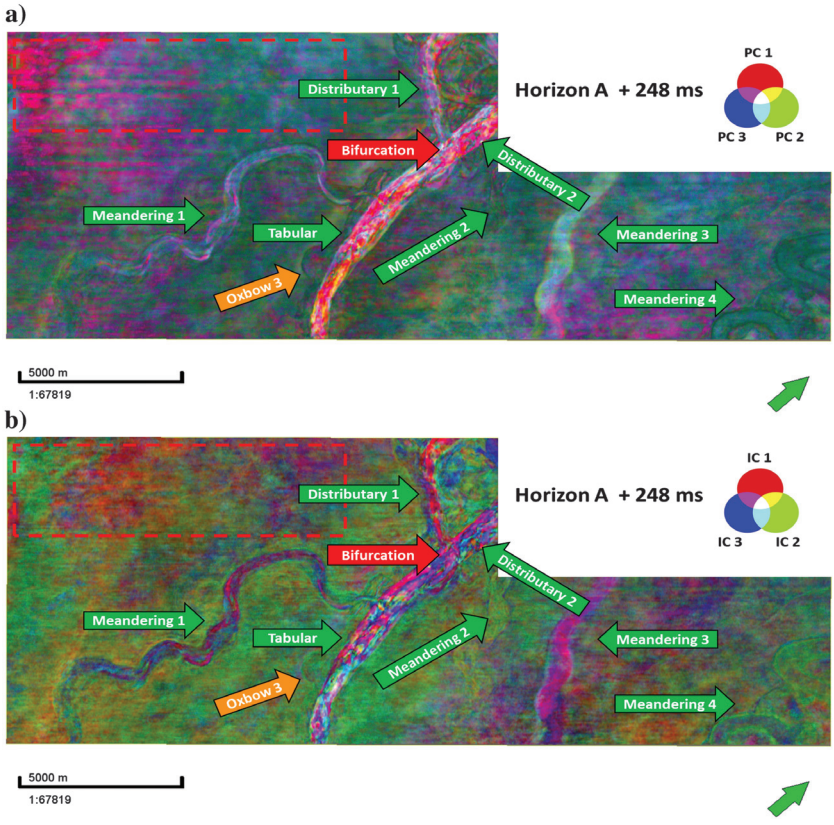


**Figure 21.** The RGB blending of PC1, PC2, and PC3 versus the RGB blending of IC1, IC2, and IC3 at phantom horizon A + 248 ms, similar colors are associated with similar seismic facies. (a) From PCA RGB blending, the large-scale meandering and tabular-shaped channels are well-delineated but the resolution decreases compared with the ICA RGB blending. In addition, the former presents a larger acquisition footprint than the latter. (b) The geologic architectural elements are better resolved in ICA RGB blending than in PCA RGB blending. The leveed meandering channel 1 is characterized predominantly by purple seismic facies intercalated with some bluish seismic facies, and the leveed meandering channel 2 is associated with a green seismic facies. The tabular-shaped channel internal architecture is highly variable with a mix of different seismic facies. The distributary channel 1 is characterized by a predominant purple seismic facies, and the distributary channel 2 looks like a prolongation of the tabular channel. Finally, the meandering channel 3 is characterized by only a purple seismic facies, and the oxbow 3 and the meandering channel 4 are characterized by a greenish infill.

Downloaded 07/31/19 to 68.97.115.26. Redistribution subject to SEG license or copyright; see Terms of Use at http://library.seg.org/

sand-rich facies. In addition, in vertical section AA′, we observe that oxbow 3, with a predominant green seismic facies related to low-amplitude reflectors, is enclosing the purple seismic facies associated with high-amplitude, continuous reflectors.

Vertical section BB′ (Figure 23b) through the meandering leveed channel 1 shows an asymmetrical configuration which, according to McHargue et al. (2011), occurs in sinusoidal channels. The fact that this channel complex is asymmetrical can be associated with cut-and-fill or waxing and waning cycles (Posamentier and Kolla, 2003). Cut-and-fill architectures can lead to upward and lateral migration of channel facies (Posamentier and Kolla, 2003). We hypothesize that in BB′ (Figure 23b), there was a first waxing and waning cycle in which sand-prone facies are deposited in the axis of the channel, whereas in the off-axis to margin of the channel, mud-prone facies are deposited (Posamentier and Kolla, 2003; McHargue et al., 2011). Then, a second waxing-waning cycle occurred, creating a cut-and-fill architecture in which the facies migrated upward and laterally (the red arrow). On the waxing and waning cycles, sand-prone facies are deposited in the axis of the channel, whereas mud-prone facies are related to off-axis to marginal deposition. In addition, in vertical section BB′, we note that axial facies associated with purple seismic facies are characterized by high-amplitude, continuous reflectors with a limited lateral extent, whereas the green seismic facies, associated with off-axis to marginal deposition, are characterized by low-amplitude reflectors as observed in section AA′. From Figure 23b, we note that the sheet sands of

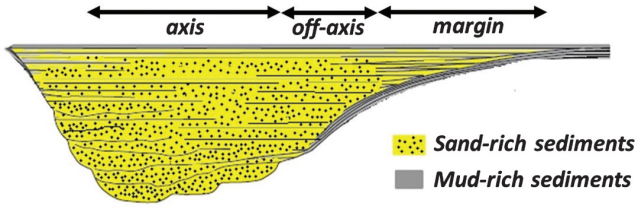


**Figure 22.** Following McHargue et al. (2011), Fildani et al. (2013), and Hubbard et al. (2014), deposition of turbiditic facies in deepwater channels can be divided into axis, off-axis, and margin. In general, the axis of the channel represents the thickest part, and it is associated with deposition of thick-bedded amalgamated sandstone facies. Off-axis to marginal deposition is characterized by interbedded sandstone and mudstone facies (heterolytic facies), implying a lower concentration of net sand. Picture after McHargue et al. (2011) and Hubbard et al. (2014).

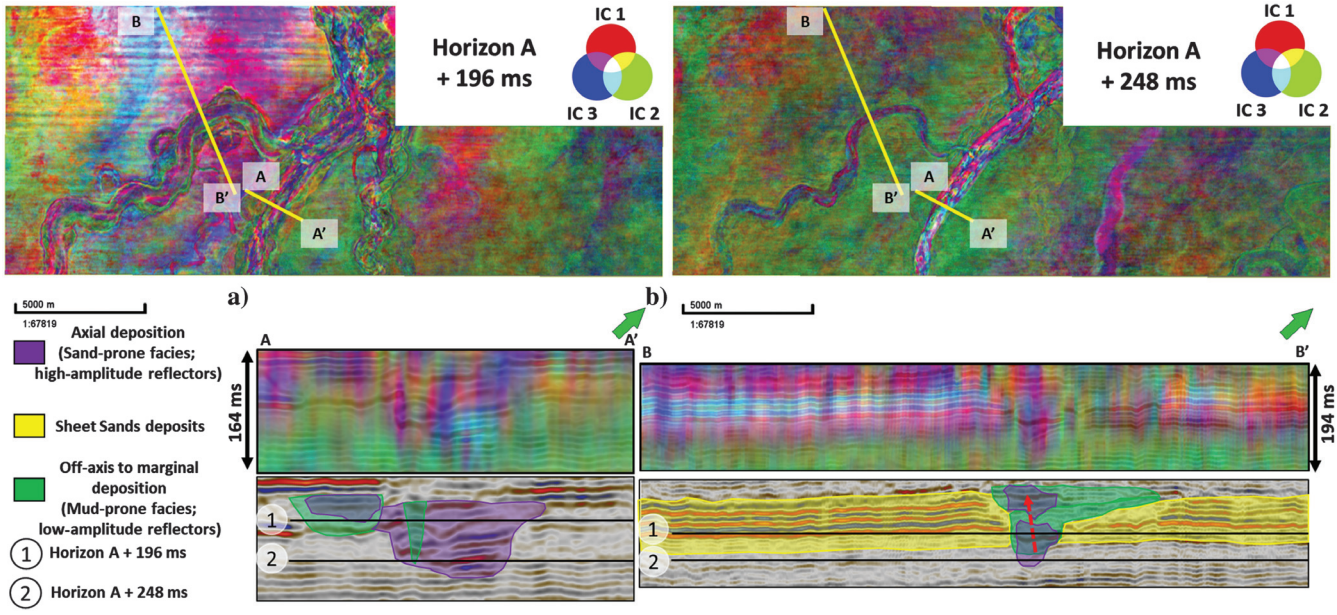


**Figure 23.** Geologic interpretation of seismic facies using ICA RGB blending and principles of geomorphology of architectural elements in deepwater channel complexes. (a) Vertical section AA′ intersecting the straight tabular-shaped channel characterized by a more variable internal architecture with predominantly purple seismic facies mixed with some green and blue facies. We interpret that this tabular-shaped channel was developed as a deep cut related to high-energy turbiditic flows during a waning cycle. In addition, weakly unconfined channels migrated inside the channel conduit. These weakly unconfined channels are characterized by a tabular shape and similar architecture to braided channels with predominantly sand-rich facies. The oxbow 3, with a predominantly green seismic facies associated with low-amplitude reflectors encloses the purple seismic facies related to high-amplitude continuous reflectors. (b) Vertical section BB′ through the meandering leveed channel 1. The sinusoidal channel is characterized by an asymmetrical configuration, which is associated with the cut-and-fill architecture. We interpret two different waxing and waning cycles in which sand-prone facies, characterized by high-amplitude reflectors, are deposited in the axis of the channel, whereas mud-prone facies, associated with low-amplitude reflectors, are related to off-axis to marginal deposition. Also, upward and lateral migration of channel facies is seen (red arrow). Sheet sands are associated with a mixture of bright-blue with yellow, red, and purple seismic facies related to high amplitude with great lateral extension parallel reflectors.

Downloaded 07/31/19 to 68.97.115.26. Redistribution subject to SEG license or copyright; see Terms of Use at http://library.seg.org/

the Moki A sands Formation are represented by a mixture of bright-blue with yellow, red, and purple seismic facies associated with high amplitude with great lateral extension parallel reflectors.

In Figure 24a, we make another vertical section CC′ through meandering leveed channel 1, but now the outer bend of the channel is facing the opposite direction. In vertical section CC′, we note that there is lateral and upward migration of facies (the red arrow); thus, cut-and-fill architecture related with waxing and waning cycles is present. Like in vertical section BB′ (Figure 23b), we hypothesize that sand-prone facies are deposited in the axis of the channel and mud-prone facies are deposited in the off-axis to marginal deposition. Moreover, purple seismic facies are still associated with axial deposition and characterized by high-amplitude continuous reflectors, whereas green purple facies with low-amplitude reflectors represent off-axis to marginal deposits. Sheet sands are associated with bright-blue seismic facies, mixed with yellow, red, and purple seismic facies.

Vertical section DD′ (Figure 24b) through meandering leveed channel 2 shows cut-and-fill architecture associated with the waxing-waning cycles. Also, we hypothesize that during channel deposition related with a second waning-waxing cycle, axial deposits from the previous waning-waxing cycle were eroded. Like in the previous observations, purple seismic facies represent high-amplitude continuous reflectors suggesting sand-prone deposits along the axis of the channel. Furthermore, green seismic facies are still characterized by low-amplitude reflectors and they represent mud-prone facies related with off-axis to marginal deposition.

Vertical section EE′ (Figure 25) through meandering channel 3 at horizon A + 248 ms shows a lateral change in the amplitude thickness that we interpret is associated with differential compaction (Chopra and Marfurt, 2012). Differential compaction is related to lateral changes in lithologies. We interpret the positive relief in EE′ as a channel filled with sand-prone sediments that do not experience as much compaction as the mud-prone facies outside it. In this case, the purple seismic facies are associated with sand-prone facies and high-amplitude reflectors and the green facies are related to mud-prone sediments and lower amplitude reflectors associated with the Moki B shale Formation.

Based on the observations made using vertical sections through the channel complexes present in the Moki A sands Formation, we hypothesize that purple seismic facies, characterized by continuous high-amplitude reflectors, are associated with sand-prone facies related to axial deposition. In contrast, we believe

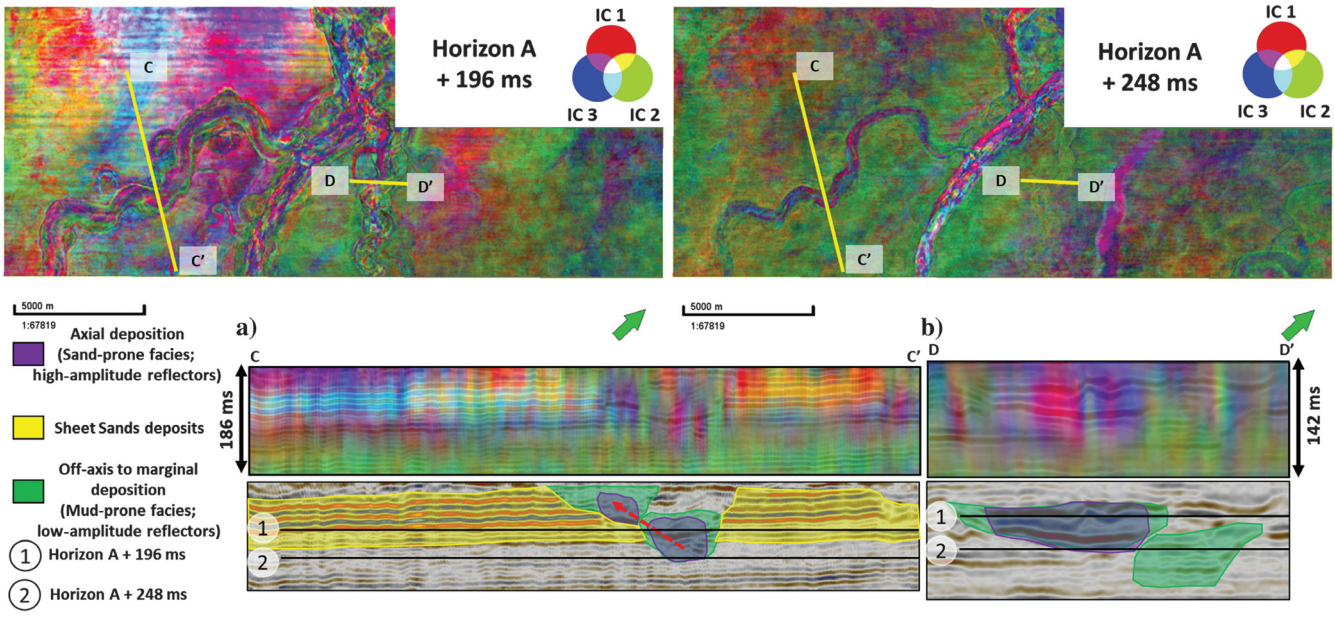


**Figure 24.** Geologic interpretation of seismic facies using ICA RGB blending and principles of geomorphology of architectural elements in deepwater channel complexes. (a) Vertical section CC′ intercepting the meandering leveed channel 1, with the outer bend of the channel facing the opposite direction compared with BB′. Cut-and-fill architectures, associated with lateral and upward migration of facies (the red arrow), are interpreted. Similar to vertical section BB′, we interpret that sand-prone facies are deposited in the axis of the channel and are characterized by purple seismic facies associated with high-amplitude continuous reflectors. Mud-prone facies deposited in the off-axis to marginal deposition are related to green purple facies characterized by low-amplitude reflectors. Finally, sheet sands are associated with bright-blue seismic facies, mixed with yellow, red, and purple seismic facies. (b) Vertical section DD′ through the meandering leveed channel 2. Cut-and-fill architectures associated with waxing-waning cycles are interpreted. We hypothesize that during channel deposition related with a second waning-waxing cycle, axial deposits from the previous waning-waxing cycle were eroded. Purple seismic facies represent high-amplitude continuous reflectors, which, based on geomorphology concepts, we believe are associated with sand-prone deposits along the axis of the channel. Green seismic facies are related to low-amplitude reflectors and represent mud-prone facies associated with off-axis to marginal deposition.



Downloaded 07/31/19 to 68.97.115.26. Redistribution subject to SEG license or copyright; see Terms of Use at http://library.seg.org/

that the green seismic facies, characterized by low-amplitude reflectors, are associated with mud-prone facies related to off-axis to marginal deposition in the meandering channel complexes. Finally, mixed blue, yellow, and red facies represent sheet sand deposits, we hypothesize that these seismic facies are associated with higher concentration of sand-prone deposits.

### *Validation of seismic facies using well data*

To validate our interpretation of the seismic facies using principles of geomorphology and the ICA RGB blending to highlight the different architectural elements, we relate the seismic facies with lithologies analyzing the gamma-ray log from the Tui SW-2 well. Figure 26 shows that high gamma-ray values associated

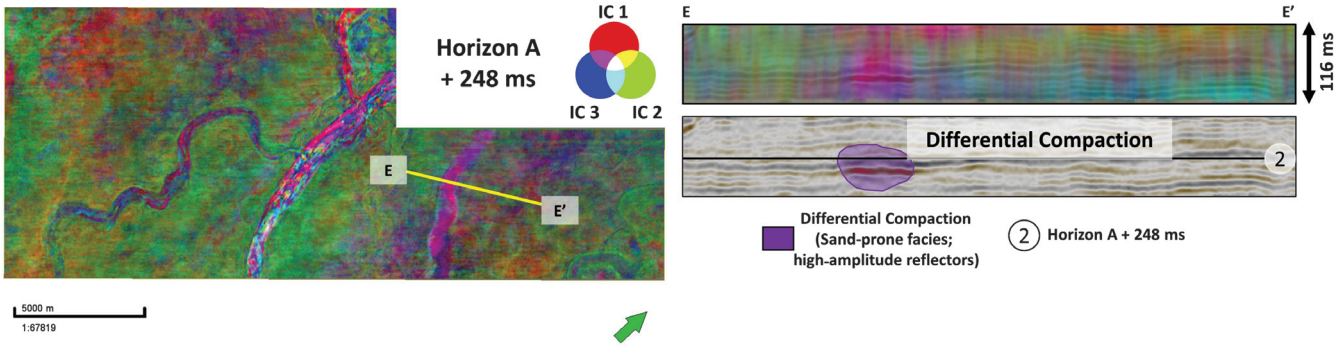


**Figure 25.** Geologic interpretation of seismic facies using ICA RGB blending and principles of geomorphology of architectural elements in deepwater channel complexes. Vertical section EE′ through meandering channel 3 at horizon A + 248 ms. There is a lateral change in the amplitude thickness, which is related to differential compaction (Chopra and Marfurt, 2012). Differential compaction is associated with lateral changes in lithologies. In this case, we interpret the positive relief as a channel filled with sand-prone sediments related to purple seismic facies, which do not experience as much compaction as the mud-prone facies of the Moki B shale Formation, associated with green seismic facies, outside it.

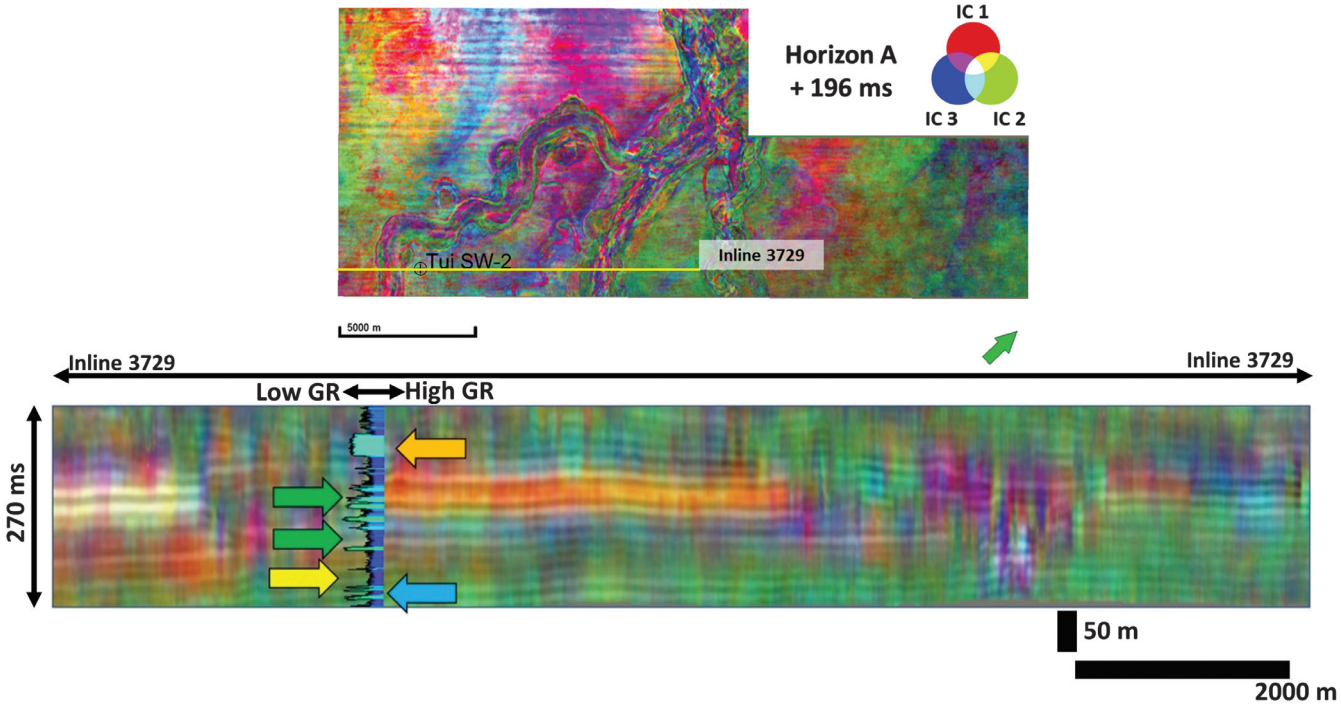


**Figure 26.** Validation of the interpretation based on the principles of geomorphology of the seismic facies in the Moki A sands Formation using the gamma-ray log from the Tui SW-2 well. High gamma-ray values associated with bathyal claystones of the Moki B shale Formation are associated with the green seismic facies (the yellow arrow), which, in our interpretation, we hypothesized were associated with mud-prone seismic facies. Small low gamma-ray values (the blue arrow) associated with calcareous sandstones are not seen in the seismic because they are below the resolution. Intercalation of high- and low-gamma-ray values associated with interbedded calcareous sandstone and claystones related to base of slope turbidites of the Moki A sands Formation are associated with the red and blue seismic facies (the green arrows), this correlate with our interpretation of sheet sands characterized by a mixture of blue, red, and yellow seismic facies. The low-gamma-ray calcareous sandstone of thickness approximate to 30 m bracketed by high-gamma-ray values associated with bathyal claystones are related with mixed purple and green seismic facies (the orange arrow).



Downloaded 07/31/19 to 68.97.115.26. Redistribution subject to SEG license or copyright; see Terms of Use at http://library.seg.org/

with bathyal claystones of the Moki B shale Formation correlate with the green seismic facies (the yellow arrow) suggesting a mud-prone seismic facies. In addition, the low gamma-ray values (the blue arrow), which are associated with calcareous sandstones, are not seen in the seismic because their thickness is approximately 5 m; thus, they are below seismic resolution. In addition, intercalation of high-gamma-ray with low-gamma-ray values associated with interbedded calcareous sandstone and claystones related to the base of slope turbidites present in the Moki A sands Formation are characterized by red and blue seismic facies (the green arrows), which is consistent with our interpretation of sheet sands characterized by a mixture of blue, red, and yellow seismic facies. Finally, the low-gamma-ray calcareous sandstone of approximate thickness of 30 m bracketed by high-gamma-ray claystone are associated with mixed purple and green seismic facies (the orange arrow) in the Tui SW-2 well. Although the Tui SW2 well is not drilled through one of the channel complexes, we believe that the validation of the seismic facies using this well can be extrapolated to the other zones of the seismic volume.

## Conclusion

Applications to a 3D seismic data volume acquired in the Taranaki Basin show that ICA is a powerful technique to reduce dimensionality, extract valuable information from multiple seismic attribute volumes, and separate geologic features from noise. ICA uses higher order statistics that found projections that were more geologic and less mathematical than PCA, in which PCs based on Gaussian statistics seem to mix multiple geologic features as well as noise. For this reason, ICA provided better resolution and better footprint reduction than PCA in this study. Small-scale geologic features characterized by lower reflectivity than large-scale geologic features are overlooked by PCA, whereas in ICA geologic features at all scales are well-preserved. Specifically, meandering and tabular-shaped tributary channels as well as abandoned meandering channels and oxbows are better delineated using ICA. Finally, ICA RGB blending provided better contrast between distinct seismic facies than PCA RGB blending. In ICA RGB blending, axial deposition associated with sand-prone facies is characterized by a distinct (the purple color in our case) seismic facies related to high-amplitude reflectors. In contrast, off-axis to marginal deposition of the channels is represented by a different (the green color) seismic facies associated with mud-prone facies and characterized by low-amplitude reflectors. Finally, sheet sand deposits are characterized by high-amplitude continuous reflectors with greater lateral extent, and they are associated with a mixture of (purple, red, and yellow) facies dominated by one (bright-blue) seismic facies.


## Acknowledgments

We thank New Zealand Petroleum and Minerals for providing the Tui3D seismic data to the public for use in research and education. Also, we would like to thank the sponsors of the Attribute Assisted Seismic Processing and Interpretation consortium for their support and to Schlumberger for the licenses in Petrel provided to the University of Oklahoma. We thank H. Posamentier, L. Infante, R. Brito, T. Ha, and E. Torres for their valuable comments.


## Data and materials availability

Data associated with this research are available and can be accessed via the following URL: https://data.nzpam.govt.nz/GOLD/system/mainframe.asp.

## Appendix A

### Preprocessing for ICA estimation

Estimation of the independent components $\mathbf{P} = \{\mathbf{P_1}, \mathbf{P_2}\}$ requires finding an unmixing matrix $\mathbf{W}$ such that its projection maximizes the independence or non-Gaussianity between the components (Hyvärinen and Oja, 2000). ICA assumes that the data have a non-Gaussian distribution.

We apply some preprocessing steps to better condition the problem. Hyvärinen and Oja (2000) suggest subtracting the mean vector $\bar{\mathbf{a}}$ of the data $\mathbf{a}$ from the value at each voxel prior to estimating the independent components. However, unlike human voices and other ICA applications, each seismic attribute may have a different unit of measurement and range of values. For example, the seismic envelope may range between 0 and +10,000, whereas the curvature may have value that range between −1 and +1 $\text{km}^{-1}$. For this reason, we apply a $Z$-score normalization to the data, i.e., subtracting its mean but also dividing by its standard deviation:

$$\mathbf{a}_n^{(\text{norm})} = (\mathbf{a}_n - \overline{\mathbf{a}_n})/\sigma(\mathbf{a}_n). \tag{A-1}$$

The next preprocessing step is to whiten the data. Whitening guarantees that the data are uncorrelated (mathematically, the covariance matrix is the identity matrix). The correlation matrix $\mathbf{C}$ is constructed by comparing each sample vector to itself and all its neighbors and can be computed from $K$ attribute volumes as

$$C_{kl} = \frac{1}{M}\sum_{m=1}^{M} \mathrm{a}_{mk}^{(\text{norm})}(t_m, x_m, y_m)\mathrm{a}_{ml}^{(\text{norm})}(t_m, x_m, y_m), \tag{A-2}$$

where $M$ is number of voxels in the volume to be analyzed.

According to Hyvärinen and Oja (2000), uncorrelated data simplify the estimation of independent components because the mixing matrix $\mathbf{A}$ becomes an orthogonal matrix, thereby reducing the number of free parameters to be computed.



Downloaded 07/31/19 to 68.97.115.26. Redistribution subject to SEG license or copyright; see Terms of Use at http://library.seg.org/

Downloaded 07/31/19 to 68.97.115.26. Redistribution subject to SEG license or copyright; see Terms of Use at http://library.seg.org/

PCA is a common technique used for dimensionality and noise reduction. The $k$th principal component $\mathbf{P}^{(k)}$ at the $m$th voxel $(t_m, x_m, y_m)$ is a scalar that represents the projection of an $N$-dimensional sample vector $\mathbf{a}$ against the $k$th unit length, $N$-dimensional eigenvector $\mathbf{v}^{(k)}$:

$$\mathbf{P}_n^{(k)}(t_m, x_m, y_m) = \sum_{n=1}^{N} \mathbf{a}_n^{(\mathrm{norm})}(t_m, x_m, y_m)\mathbf{v}_n^{(k)}. \quad \text{(A-3)}$$

PCA can be used to whiten the data. Specifically, after computing the principal components $\mathbf{P_n}$, we rescaled them by $1/\sqrt{\lambda_n}$ thereby making each of the projections have unit variance:

$$\mathbf{a}_n^{(w)} = \frac{\mathbf{P}_n^{(k)}(t_m, x_m, y_m)}{(\lambda_n + \varepsilon)^{1/2}}, \quad \text{(A-4)}$$

where $\mathbf{a}_n^{(w)}$ represents the data after $Z$-score normalization and whitening, $\lambda_n$ are the eigenvalues of the correlation matrix, and $\varepsilon$ is a fraction of the largest eigenvalue $\lambda_1$, to avoid division by zero.

Using PCA whitening, we not only reduce the dimensionality of the data but also reduce noise during the independent component estimation (Hyvärinen and Oja, 2000). To decide how many components we should preserve, we analyze the percentage of variance retained (Stanford, 2018).

If we have $N$ principal components, the eigenvalues are $\lambda_1, \lambda_2, \lambda_3, \ldots, \lambda_N$, where $\lambda_n \geq \lambda_{n+1}$. For $N$ attributes, Stanford (2018) suggests keeping the largest $K$ components whose sum just exceeds a user-defined percentage $\beta$ of the variability $E$ of the data, where the remaining variability is considered to be noise:

$$\frac{\sum_{n=1}^{K} \lambda_n}{\sum_{n=1}^{N} \lambda_n} \geq \beta, \quad \text{(A-5)}$$

where we use a value $\beta = 0.9$ to define the data from noise.

## The ICA algorithm

Based on the central limit theorem, Hyvärinen and Oja (2000) state that the distribution of two independent variables is less Gaussian than the distribution of the sum of the two variables. Therefore, by maximizing the non-Gaussianity of the preprocessed data, we can find the unmixing matrix $\mathbf{W}$ that maximizes the independence of the sources $\mathbf{P_1}$ and $\mathbf{P_2}$.

Because a Gaussian variable has the largest entropy of all, Hyvärinen and Oja (2000) quantitatively measure non-Gaussianity based on an approximation of negentropy, which is a modified version of entropy that is always nonnegative and is equal to zero for a Gaussian distribution.

Assuming a random variable $\mathbf{y} = \mathbf{W}^{\mathrm{T}}\mathbf{a}^{(\mathrm{w})}$ with zero mean and unit variance, Hyvärinen (1999) approximates the negentropy $J$ as

$$J(y) = \{E[G(y)] - E[G(v)]\}^2, \quad \text{(A-6)}$$

where $G$ is a nonquadratic function called the contrast function, $v$ is a centered and whitened Gaussian variable, and $E$ is the expected value operator. In practice, the expectation operator must be replaced by the sample means (Hyvärinen and Oja, 2000).

To compute the independent components, Hyvärinen and Oja (2000) develop an algorithm called FastICA, in which the goal is to maximize the contrast function $G$. Any nonquadratic function can be used in the computations (Hyvärinen and Oja, 2000). We follow Honorio et al. (2014), and use the contrast function:

$$G(y) = -e^{-(y^2/2)}, \quad \text{(A-7)}$$

which through empirical analysis appears to provide good resolution and delineation of the geologic features. The independent components are computed simultaneously. To avoid convergence to the same maxima, the outputs are decorrelated after each iteration (Hyvärinen and Oja, 2000).

Following Hyvärinen and Oja (2000), in each iteration of the algorithm, each row of the unmixing matrix $\mathbf{W}$ is updated by

$$\mathbf{W_j^+} = E\left[\mathbf{a}^{(w)}\frac{\partial G}{\partial y}(\mathbf{W_j^T}\mathbf{a}^{(\mathbf{w})})\right] - E\left[\frac{\partial^2 G}{\partial^2 y}(\mathbf{W_j^T}\mathbf{a}^{(\mathbf{w})})\right]\mathbf{W_j}, \quad \text{(A-8)}$$

and normalized by

$$\mathbf{W_j^+} = \mathbf{W_j^+}/\|\mathbf{W_j^+}\|, \quad \text{(A-9)}$$

where $\mathbf{W}^+$ is the updated unmixing matrix. Finally, the updated unmixing matrix $\mathbf{W}^+$ is decorrelated using eigenvalue decomposition by

$$\mathbf{W}_{\mathrm{decorr}}^{+} = (\mathbf{W}\mathbf{W}^{\mathbf{T}})^{-1/2}\mathbf{W}. \quad \text{(A-10)}$$

Convergence is reached when the dot product between the old and new values of $\mathbf{W}$ is close to one, indicating that they are parallel and unchanged (Hyvärinen and Oja, 2000).

Finally, the energy of each independent component is the sum of the energy over all the voxels that fall in the target region:

$$L = \sum_{m=1}^{M} y_i(t_m, x_m, y_m)^2, \quad \text{(A-11)}$$

where $y_i(t_m, x_m, y_m)$ is the $i$th independent component at voxel $m$ and $M$ is the number of voxels in the target area.

## References

Aires, F., A. Chédin, and J. P. Nadal, 2000, Independent component analysis of multivariate series: Application to the tropical SST variability: Journal of Geophysical Research, **105**, 17437–17455, doi: 10.1029/2000JD900152.

Bussell, M. R., 1994, Seismic interpretation of the Moki Formation on the Maui 3D survey, Taranaki Basin: New Zealand Petroleum Conference Proceedings, Ministry of Economic Development, 240–255.
Chopra, S., and K. J. Marfurt, 2012, Seismic attribute expression of differential compaction: 82nd Annual International Meeting, SEG, Expanded Abstracts, doi: 10.1190/segam2012-1323.1.
Chopra, S., and K. J. Marfurt, 2014, Churning seismic attributes with principal component analysis: 84th Annual International Meeting, SEG, Expanded Abstracts, 2672–2676, doi: 10.1190/segam2014-0235.1.
Chopra, S., and K. J. Marfurt, 2015, Choice of mother wavelets in CWT spectral decomposition: 85th Annual International Meeting, SEG, Expanded Abstracts, 2957–2961, doi: 10.1190/segam2015-5852193.1.
Chopra, S., and K. J. Marfurt, 2016, Spectral decomposition and spectral balancing of seismic data: The Leading Edge, **35**, 176–179, doi: 10.1190/tle35020176.1.
Coléou, T., M. Poupon, and K. Azbel, 2003, Unsupervised seismic facies classification: A review and comparison of techniques and implementation: The Leading Edge, **22**, 942–953, doi: 10.1190/1.1623635.
Dauzacker, M. V., J. S. Yang, G. A. Pomilio, and V. S. Till, 1996, A new exploratory approach to the Moki-Manaia oil discoveries: New Zealand Petroleum Conference Proceedings, 86–104.
De Bock, J. F., 1994, Moki formation, a Miocene reservoir sequence, its facies distribution and source in offshore, southern Taranaki Basin: New Zealand Petroleum Conference Proceedings, 155–167.
Engbers, P., 2002, Evaluation of Moki sands prospectivity in Maui PML: New Zealand Petroleum Conference Proceedings, Ministry of Economic Development.
Fildani, A., S. M. Hubbard, J. A. Covault, K. L. Maier, B. W. Romans, M. Traer, and J. C. Rowland, 2013, Erosion at inception of deep-sea channels: Marine and Petroleum Geology, **41**, 48–61, doi: 10.1016/j.marpetgeo.2012.03.006.
Guo, H., K. J. Marfurt, and J. Liu, 2009, Principal component spectral analysis: Geophysics, **74**, no. 4, P35–P43, doi: 10.1190/1.3119264.
Hansen, R. J., and P. J. Kamp, 2006, An integrated biostratigraphy and seismic stratigraphy for the late Neogene continental margin succession in northern Taranaki Basin, New Zealand: New Zealand Journal of Geology and Geophysics, **49**, 39–56, doi: 10.1080/00288306.2006.9515146.
Honorio, B., A. Sanchetta, E. Pereira, and A. Vidal, 2014, Independent component spectral analysis: Interpretation, **2**, no. 1, SA21–SA29, doi: 10.1190/INT-2013-0074.1.
Hubbard, S. M., J. A. Covault, A. Fildani, and B. W. Romans, 2014, Sediment transfer and deposition in slope channels: Deciphering the record of enigmatic deep-sea processes from outcrop: Geological Society of America Bulleting, **126**, 857–871, doi: 10.1130/B30996.1.
Hyvärinen, A., 1999, Survey of independent component analysis: Neural Computing and Applications, **2**, 94–128.
Hyvärinen, A., 2012, Independent component analysis: Recent advances: Philosophical Transactions of the Royal Society A, **371**, 20110534, doi: 10.1098/rsta.2011.0534.
Hyvärinen, A., and E. Oja, 2000, Independent component analysis: Algorithms and applications: Neural Networks, **13**, 411–430, doi: 10.1016/S0893-6080(00)00026-5.
Infante-Paez, L., 2018, Seismic expression of igneous bodies in sedimentary basins and their impact on hydrocarbon exploration: Examples from a compressive tectonic setting, Taranaki Basin, New Zealand: Ph.D. dissertation, University of Oklahoma.
Infante-Paez, L., and K. Marfurt, 2017, Seismic expression and geomorphology of igneous bodies: A Taranaki Basin, New Zealand, case study: Interpretation, **5**, no. 3, SK121–SK140, doi: 10.1190/INT-2016-0244.1.
Kim, K.-Y., and Q. Wu, 1999, A comparison study of EOF techniques: Analysis of nonstationary data with periodic statistics: Journal of Climate, **12**, 185–199, doi: 10.1175/1520-0442-12.1.185.
King, P. R., G. H. Scott, and P. H. Robinson, 1993, Description, correlation and depositional history of Miocene sediments outcropping along North Taranaki coast: Institute of Geological and Nuclear Sciences Ltd., 199.
King, P. R., and G. P. Thrasher, 1996, Cretaceous Cenozoic geology and petroleum systems of the Taranaki Basin, New Zealand: Institute of Geological and Nuclear Sciences 2.
Kohonen, T., 1982, Self-organized formation of topologically correct feature maps: Biological Cybernetics, **43**, 59–69, doi: 10.1007/BF00337288.
Li, F., and W. Lu, 2014, Coherence attribute at different spectral scales: Interpretation, **2**, no. 1, SA99–SA106, doi: 10.1190/INT-2013-0089.1.
Li, F., J. Qi, B. Lyu, and K. J. Marfurt, 2018, Multispectral coherence: Interpretation, **6**, no. 1, T61–T69, doi: 10.1190/INT-2017-0112.1.
Li, Y., X. Zheng, and J. Li, 2009, Dimensionality reduction and feature extraction from seismic spectral decomposed data using independent component analysis: CPS/SEG International Geophysical Conference and Exposition.
Lubo-Robles, D., and K. J. Marfurt, 2017, Delineation of thick incised canyons using spectral-decomposition analysis, curvature and self-organizing maps in the Exmouth plateau, Australia: 87th Annual International Meeting, SEG, Expanded Abstracts, 2420–2424, doi: 10.1190/segam2017-17790008.1.
Ma, Z., 2011, Non-Gaussian statistical models and their applications: Ph.D. dissertation, KTH Royal Institute of Technology.
MacQueen, J., 1967, Some methods for classification and analysis of multivariate observations: Proceedings of the 5th Berkeley Symposium on Mathematical Statistics and Probability, 1, 281–297.

Downloaded 07/31/19 to 68.97.115.26. Redistribution subject to SEG license or copyright; see Terms of Use at http://library.seg.org/

Marfurt, K. J., 2018, Seismic attributes as the framework for data integration throughout the Oilfield Life Cycle: SEG, Distinguished Instructor Series 21.
Marfurt, K. J., and R. L. Kirlin, 2001, Narrow-band spectral analysis and thin-bed tuning: Geophysics, **66**, 1274–1283, doi: 10.1190/1.1487075.
McHargue, T., M. J. Pyrcz, M. D. Sullivan, J. D. Clark, A. Fildani, B. W. Romans, J. A. Covault, M. Levy, H. W. Posamentier, and N. J. Drinkwater, 2011, Architecture of turbidite channel systems on the continental slope: Patterns and predictions: Marine and Petroleum Geology, **28**, 728–743, doi: 10.1016/j.marpetgeo.2010.07.008.
Palmer, J., 1985, Pre-miocene lithostratigraphy of Taranaki Basin, New Zealand: New Zealand Journal of Geology and Geophysics, **28**, 197–216, doi: 10.1080/00288306.1985.10422220.
Partyka, G., J. Gridley, and J. Lopez, 1999, Interpretational applications of spectral decomposition in reservoir characterization: The Leading Edge, **18**, 353–360, doi: 10.1190/1.1438295.
Pilaar, W. F. H., and L. L. Wakefield, 1984, Hydrocarbon generation in the Taranaki Basin, New Zealand, *in* G. Demaison and R. J. Murris, eds., Petroleum geochemistry and basin evaluation: AAPG special volumes **M35**, 405–423.
Posamentier, H. W., and V. Kolla, 2003, Seismic geomorphology and stratigraphy of depositional elements in deep-water settings: Journal of Sedimentary Research, **73**, 367–388, doi: 10.1306/111302730367.
Roden, R., T. Smith, and D. Sacrey, 2015, Geologic pattern recognition from seismic attributes: Principal component analysis and self-organizing maps: Interpretation, **3**, no. 4, SAE59–SAE83, doi: 10.1190/INT-2015-0037.1.
Roy, A., S. R. Araceli, J. T. Kwiatkowski, and K. J. Marfurt, 2014, Generative topographic mapping for seismic facies estimation of a carbonate wash, Veracruz basin, Southern Mexico: Interpretation, **2**, no. 1, SA31–SA47, doi: 10.1190/INT-2013-0077.1.
Shlens, J., 2014, A tutorial on independent component analysis: arXiv:1404.2986.
Sinha, S., D. Devegowda, and B. Deka, 2016, Multivariate statistical analysis for resource estimation in unconventional plays application to Eagle Ford shales: Presented at the SPE, doi: 10.2118/184050-MS.
Sinha, S., P. Routh, P. Anno, and J. Castagna, 2005, Spectral decomposition of seismic data with continuous-wavelet transform: Geophysics, **70**, no. 6, P19–P25, doi: 10.1190/1.2127113.
Stanford, 2018, PCA Whitening, http://ufldl.stanford.edu/tutorial/unsupervised/PCAWhitening/, accessed 26 March 2018.
Strecker, U., and R. Uden, 2002, Data mining of 3D poststack attribute volumes using Kohonen self-organizing maps: The Leading Edge, **21**, 1032–1037, doi: 10.1190/1.1518442.
Thrasher, G., 1992, Late Cretaceous geology of Taranaki Basin, New Zealand: Ph.D. dissertation, Victoria University of Wellington.
Thrasher, G. P., B. Leitner, and A. W. Hart, 2002, Petroleum system of the Northern Taranaki Graben: New Zealand Petroleum Conference Proceedings, Ministry of Economic Development.
Tibaduiza, D. A., L. E. Mujica, M. Anaya, J. Rodellar, and A. Gemes, 2012, Principal component analysis vs. independent component analysis for damage detection: 6th European Workshop on Structural Health Monitoring.
Veritas DGC, Australia Pty. Ltd/New Zealand Overseas Petroleum Ltd, 2003, Tui-3D seismic survey: Ministry of economic development New Zealand, unpublished petroleum report, PR2830.
Walden, A. T., 1985, Non-Gaussian reflectivity, entropy, and deconvolution: Geophysics, **50**, 2862–2888, doi: 10.1190/1.1441905.
Yagci, G., 2016, 3D seismic structural and stratigraphic interpretation of the Tui-3D field, Taranaki Basin, New Zealand: M. S. thesis, Missouri University of Science and Technology.
Zhao, T., V. Jayaram, A. Roy, and K. J. Marfurt, 2015, A comparison of classification techniques for seismic facies recognition: Interpretation, **3**, no. 4, SAE29–SAE58, doi: 10.1190/INT-2015-0044.1.
Zhao, T., F. Li, and K. J. Marfurt, 2016, Advanced self-organizing map facies analysis with stratigraphic constraint: 86th Annual International Meeting, SEG, Expanded Abstracts, 1666–1670, doi: 10.1190/segam2016-13949728.1.

**David Lubo-Robles** received a bachelor's degree in geophysical engineering from Simon Bolivar University, Venezuela, and a master's degree in geophysics from the University of Oklahoma under Kurt J. Marfurt. He is a student member of SEG and is currently pursuing a doctorate in geophysics at the University of Oklahoma, studying under Kurt J. Marfurt and Matthew Pranter. His research interests include the development and application of modern machine-learning and pattern-recognition techniques, together with quantitative interpretation skills, including prestack inversion and seismic attribute analysis to delineate geologic features amenable to hydrocarbon accumulation.

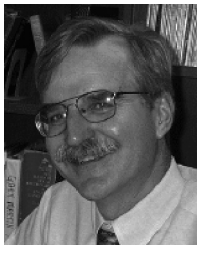

**Kurt J. Marfurt** began his geophysical career teaching geophysics and contributing to an industry-supported consortium on migration, inversion, and scattering (project MIDAS) at Columbia University's Henry Krumb School of Mines in New York City. In 1981, he joined Amoco's Tulsa Research Center and spent the next 18 years leading research efforts in modeling, migration, signal analysis, basin analysis, seismic attribute analysis,

Downloaded 07/31/19 to 68.97.115.26. Redistribution subject to SEG license or copyright; see Terms of Use at http://library.seg.org/

reflection tomography, seismic inversion, and multicomponent data analysis. In 1999, he joined the University of Houston as a professor in the Department of Geosciences and as a director of the Allied Geophysics Laboratories. He is currently a member of the Geophysical Societies of Tulsa and Houston, SEG, EAGE, AAPG, AGU, and SIAM, and he serves as Deputy Editor-in-Chief for *Interpretation*. His current research activity includes prestack imaging, velocity analysis and inversion of converted waves, computer-assisted pattern recognition of geologic features on 3D seismic data, and interpreter-driven seismic processing. His research interests include seismic signal analysis, 3D seismic attributes, seismic velocity analysis, subsurface imaging, and multicomponent data analysis.

Downloaded 07/31/19 to 68.97.115.26. Redistribution subject to SEG license or copyright; see Terms of Use at http://library.seg.org/